

**Point-by-Point Response to Referee Comments, Including Relevant Changes Made in the Manuscript, and Marked-Up Manuscript**

**J. S. Wang et al.**

Our responses below are in **boldface**. In the responses, we note the relevant changes made in the manuscript.

Anonymous Referee #1

1 General comments

Overall a good paper, well structured and written, which proposes a useful analysis of the constraints brought by future remote-sensing CO<sub>2</sub> measurements with high spatiotemporal resolution on regional-scale CO<sub>2</sub> fluxes. It also presents an interesting discussion about the target and threshold requirements to answer key carbon cycle questions (Section 4). One concern is that while the authors point out the limitations of the method used, and in particular the impact of assuming perfect boundary conditions or incorrect prior error statistics, they do not try to assess (at least partially) the sensitivity of their results to those assumptions. This would be especially interesting here since the high spatiotemporal density of the ASCENDS observations could actually result in the inversion being only weakly sensitive to the prior information. In addition, the explanations for the difference in posterior errors obtained with the global inversion and the regional one are not always well explained. This question of inversion technique, while interesting, is somewhat tangential to the main question of instrument design, and seems to raise more questions than answers, so the authors might consider removing section 3.2 and saving the topic for more complete treatment at a later date.

**We thank the referee for the detailed and constructive comments. We now report results of sensitivity tests addressing the issues of boundary conditions and prior uncertainty assumptions (Section 4.2). A simple test inversion in which b.c. are added as solved-for parameters suggests that flux uncertainty reductions decrease slightly when b.c. uncertainties are accounted for; however, we acknowledge that the exact magnitude of the effect could very much depend on the experimental setup. Another new sensitivity test demonstrates that the posterior uncertainty in many locations is not very sensitive to the prior uncertainty and is strongly influenced by the observations. (Note that we have moved the material on the a priori error correlation sensitivity test from the original Sections 3.1 and 3.3 to the new Section 4.2.)**

**Also, in light of this reviewer's opinion together with that of the second reviewer, we have decided to greatly abbreviate the material comparing the regional OSSE results with the global OSSE's (Section 3.2) and combine it with the material in the original Section 3.3. We now show the global inversion results only aggregated to the biome level (as well as the results of Gourdji et al. [2012]), mainly to provide context for our regional inversion results rather than to quantitatively analyze effects of various methodological differences.**

**Note that we have revised the global inversion results to correct an error in the calculation of observation uncertainties and also an error in the boundary layer vertical mixing in the transport model (both of these errors were specific to the global inversion and not to the regional inversion). The corrected results, shown in the new Figure 10, are not drastically different from the original results, and the difference does not affect our conclusions.**

2 Detailed comments

•

p. 12823, l. 6-8: I don't follow this explanation. In both the Eulerian and the Lagrangian simulations interpolated meteorological fields are used. The ability of the Lagrangian model to better simulate filamentation processes compared to the Eulerian one stems from the strong diffusion/dilution effects when using Eulerian simulations with coarse resolution.

**Our original explanation was indeed inaccurate. The comparison should be between particle dispersion models and gridded transport models rather than between Lagrangian and Eulerian models.**

**We have modified the explanation, as well as mentioning the diffusion effects of gridded models that the reviewer points out.**

•

p. 12822, l. 18: Also, Deng et al., ACP, 2014.

**Done.**

•

p. 12823, l. 12-16: Articles from Brioude et al. (2011, 2012) (maybe some others from the same author) should be cited here.

**We now cite those two papers as well as Brioude et al. [2013].**

•

p. 12824, l. 14: "...uncertainty levels in constraining the fluxes that ASCENDS observations..."

**Done (with a slight modification to the reviewer's suggested wording).**

•

p. 12826, l. 10-11: It is not very clear what "...the measurements errors at each location are scaled to two possible performance levels: 0.5 ppm and 1.0 ppm error..." means. Do you use only those constant error values in this study (with differences only due to the number of observations within each pixel)? It seems like from the reading of the next sections, but it should be better clarified here.

**No, the error for each observation is not constant, but a function of OD and surface backscatter data, as described in the preceding sentences. Those values are scaled to reference 10-s average error levels for a particular set of conditions: OD = 0 and surface reflectivity equal to that at Railroad Valley, Nevada. We have now improved the text to clarify that.**

•

p. 12830, l. 16: Not clear over what the average is done here.

**We now provide additional explanation: the footprints are averaged for all the 5-km receptor locations that fall within a 10-s averaging period along the satellite track. In an earlier section (2.2), we've also added the distance corresponding to that interval: 67 km.**

•

Section 3.1: I think this section should be simplified a bit. The posterior error reduction always results from the combined effects of the observation sensitivities (Jacobian), observational errors, and prior errors. Here the authors focus on describing the relative contribution of each of them to explain the uncertainty patterns observed. I would rather put more emphasis on the implication of the error reduction spatial distributions in term of constraints on specific CO<sub>2</sub> sources/sinks sectors for instance.

**We have now simplified this section, and de-emphasized statements identifying the contributors to uncertainty reduction, given that that knowledge is already well established. Regarding specific sources and sinks, in the following section (3.2), we do discuss the implications of the error reductions for constraining fluxes from particular biomes, such as tundra or Eastern temperate forest. Also, we compare flux constraints for different seasons in both this section and the next.**

•

p. 12831, l.6: The recent satellite-based regional CH<sub>4</sub> inversion by Wecht et al. (JGR, 2014) discusses and treats the issue of boundary conditions explicitly. This aspect is a critical factor in the derivation of regional constraints for CH<sub>4</sub>, and thus one must assume that it is an even greater factor for CO<sub>2</sub>. That the issue is only raised here as part of the discussion of uncertainty in 4.2, but not factored into the actual results, is of considerable concern. At the very least, this potentially large limitation should be mentioned in the abstract to qualify the estimated inversion performance.

**We have now added a sensitivity test for b.c. (See response to general comments above.) We now also mention the sensitivity of our results to b.c. and other assumptions in the abstract.**

•

p. 12833, l. 27-28: I don't agree with this statement: "The reason for this is that longer a priori error correlation lengths result in fewer "unknowns" to be constrained by the observations". Longer error correlations essentially better transfer

the observational information throughout the control vector elements (the fluxes here), which results in stronger constraints for each flux in average. Although it mechanically results in fewer "unknowns" to be solved for, saying the latter is the cause for the larger uncertainty reduction is confusing I think.

**We have removed that sentence. We keep the sentence that followed that one, which is consistent with the reviewer's preferred explanation.**

•

p. 12834, l.18: Please specify what model is used here.

**We've now specified the model, PCTM [Kawa et al., 2004], in Section 3.2, 2<sup>nd</sup> paragraph.**

•

p. 12834, l.26-28: Are you using the method described in Chevallier et al. (2012) (Appendix B)? If yes, please explicitly refer to this paper.

**No, our method for aggregating variances is based on general statistical methods, not specifically a method described in a particular paper.**

•

p. 12835, l.10: It would be good to explain what is the basic principle of this (estimate-truth) statistics methodology.

**Now that we have de-emphasized the comparison of the regional OSSE with the global one, we do not feel that it is appropriate to include too much text describing the global OSSE methodology. We do, however, include in the new section, "Results Aggregated to Biomes and Continent, and Compared with Other Inversion Systems" (3.2), a reference to the paper by Baker et al. [2010] that provides the methodological details.**

•

p. 12835, l.12: "in results" <-> "in error reductions"

**We have deleted most of the section containing this sentence.**

•

p. 12835, l. 11-28: The explanations given for the higher error reductions obtained with the global inversion compared to the regional one are not clear. Are the models/meteorological fields used in both simulations the same (could have a great impact)? How much might the different means of calculating (Lagrangian) versus estimating (variational) the uncertainties play a role? Assuming the same model is used, and that only the resolution is different from the two inversions, the only scale-dependent errors I can see are the aggregation errors (the authors should cite and refer to Bocquet et al. (2011) here for the definition of this concept). Assuming the observation information is the same (i.e. same errors), an increase in uncertainty reduction could happen if the aggregated prior errors are higher than those at fine resolution for instance. I think the authors need to substantially expand upon their explanations here, or consider removing this section.

**As described above in our response to the general comments, we have now deleted much of this section, and we now show the global inversion results only aggregated to the biome level, mainly to provide context for our regional inversion results rather than to quantitatively analyze effects of various methodological differences.**

**As the referee suggested, we have added a citation of Bocquet et al. [2011] in discussing aggregation error (in the Introduction section rather than in the text on the global inversion that no longer exists).**

•

p. 12836, l. 15 -17: Not necessary.

**We have deleted that sentence.**

•

p. 12837, l.23: "... the comparison is not totally consistent..."

**We've made that change.**

•

p. 12838, l.23-end: That's a good point. However, it would be useful to quantify explicitly the relative contribution of the observational information to the meeting of the target requirement (i.e. where is the prior error already very close to the target level?). A map showing this relative contribution might be useful here.

**We've added a plot in the current Figure 10 (panel e) that shows the fractional uncertainty reduction necessary for each biome to meet the target requirement. This is one way to quantify the contribution of the observations to meeting the target, ranging from 0 for desert (where the prior uncertainty is already at the target) to 85% for eastern temperate, with most of the amounts being greater than 50%. We do not feel that a map is necessary, given that this is a biome-scale target rather than a grid-scale target.**

•  
Section 4.2: Given the high spatiotemporal density of the ASCENDS data, it would be interesting to assess how much the uncertainty reduction depend on the prior errors, which are often incorrectly specified. I think it is a key question in general for such inversions to understand how much we depend on our prior information.

**We have now added a sensitivity test for prior uncertainties. (See response to general comments above.)**

•  
p. 12842, l. 7: for all wavelengths?

**Yes, this quantity is an average over the two wavelengths. We've added text that explains this explicitly.**

•  
p. 12842, l.11-12: "... it has fewer unknowns to be solved for...". Again, this argument is not clear.

**Most of the text on the comparison of the regional and global inversions, including this paragraph, has been deleted.**

•  
p. 12842, l.24-28: Although this could be left for future investigations, I think testing at least 2 different sets of boundary conditions as well as two different prior error scenarios would strengthen this study.

**We've added sensitivity tests on b.c. and prior uncertainties, as described above.**

•  
Figure 3: What is F here? One could think F is the flux and therefore  $\sigma = F$  unitless. Please clarify.

**We've now added the definition,  $F \equiv \text{flux}$ , in the caption.**

Anonymous Referee #2

This study used Observation System Simulation Experiments to assess impacts from the ASCENDS observations on top-down regional flux estimates. In particular, it highlighted the potential for inferring flux estimates at high temporal and spatial resolutions from dense space-borne XCO<sub>2</sub> observations. It is well written, and I recommend it for publication after some modifications.

**We thank the referee for the constructive comments.**

Major comments:

1. Instead of the complete flux inversions, only the error reductions have been calculated in this study. So, it did not fully assess the ability for their flux inversion system to recover the 'true' regional fluxes by assimilating ASCENDS observations. For example, the possible adverse effects from errors in boundary conditions and errors in model transport have not been quantitatively investigated, although they have provided some interesting discussions in Section 4.

**We do acknowledge in the manuscript that we did not conduct complete inversions and chose to focus on uncertainty reduction brought about by the measurements, assumed to be free of systematic errors. This type of analysis can be accomplished without the use of a complete inversion, and can be considered separately from the effect of transport errors, which are a type of systematic error. (We qualitatively discuss systematic errors in Section 4.3.) Furthermore, related studies have demonstrated the ability to recover "true" fluxes from observations. For example, Gourdji et al. [2010] conducted a full inversion over North America at the same spatial resolution for fluxes as our study and using the same transport model, WRF-STILT, although they used a different data set (tower**

network). As another example, a global OSSE that is a companion to our regional OSSE involved a full inversion using synthetic ASCENDS observations. Regarding boundary condition errors, we have now added a sensitivity test on b.c. in Section 4.2.

2. I am not sure whether the comparisons with the error reductions in global flux inversion experiments have significantly enhanced the main discussions. Instead I'd like to see, to which extent the global flux inversions based on ASCENDS measurements could reduce boundary condition errors as discussed in Section 4.2.

**We have de-emphasized the comparison of the regional and global OSSE results, as described in our response to the general comment of Referee #1 above. As for the suggestion to demonstrate the ability of a global ASCENDS inversion to reduce boundary condition errors for a regional inversion, we agree that that would be an informative analysis. However, we see it as lying outside the focus area of our regional OSSE, and worthy of presentation in a separate paper. What is more directly relevant for our paper is how b.c. errors translate to regional flux errors. We have addressed this issue to a certain extent through a new sensitivity test in Section 4.2. Assessing the impact of systematic errors in b.c. would require additional analysis.**

Minor Comments:

1. Page 12824, Line 21: 'Kx=c, where x is the vector of fluxes, and c denotes concentrations',

This statement is not accurate as the definition of the Jacobian, as the concentrations also have contributions from background or in-flows etc.

**Good point. We have changed the definition so that it no longer contains that misleading equation and instead refers to the sensitivity of concentrations to changes in the state vector elements.**

2. Page 12826, line 13: 'The errors for 5km (0.74s) individual CALIPSO ...',  
What is the footprint size for the aggregated 10s observations ?

**We've added that piece of information: 67 km.**

3. Page 12834, line 23: ', and the assumption of zero a priori correlation ...',  
Are the temporal error correlations of a priori flux estimates set to be zero as well ?

**Yes, temporal error correlations are zero. We have now removed the parenthetical about the coarser spatial scale that led to the reviewer's question.**

4. Page 12835, line 16: 'Thus in our inversion, less information is available ...'.

The phrase of 'less information' can be misleading.

**We have actually deleted most of the material in this section (comparison of regional and global OSSEs at grid scale), including that sentence.**

5. Page 12852, Caption:  $(10^{-6} \text{ ppmv}^{-1} \text{ hPa}^{-1})$

Is this unit  $(\text{ppmv}^{-1})$  right ?

**Yes, it's right. We've added the phrase "per ppmv of CO<sub>2</sub>" after the term "Vertical weighting functions".**

1 **A Regional CO<sub>2</sub> Observing System Simulation Experiment for the ASCENDS Satellite**

2 **Mission**

3  
4 James S. Wang,<sup>1,2</sup> S. Randolph Kawa,<sup>2</sup> Janusz Eluszkiewicz,<sup>3,\*</sup> David F. Baker,<sup>4</sup> Marikate  
5 Mountain,<sup>3</sup> John Henderson,<sup>3</sup> Thomas Nehrorn,<sup>3</sup> and T. Scott Zaccheo<sup>3</sup>

6  
7  
8 <sup>1</sup>Universities Space Research Association, Columbia, MD, USA, james.s.wang@nasa.gov

9 <sup>2</sup>NASA Goddard Space Flight Center, Greenbelt, MD, USA

10 <sup>3</sup>Atmospheric and Environmental Research, Lexington, MA, USA

11 <sup>4</sup>Cooperative Institute for Research in the Atmosphere, Colorado State University, Fort Collins,

12 CO, USA

13 <sup>\*</sup>Deceased as of 27 May 2014

Formatted: Superscript

14  
15  
16  
17  
18  
19  
20  
21 ~~Accepted for publication~~Under review in *Atmospheric Chemistry and Physics* ~~Discussions~~

22

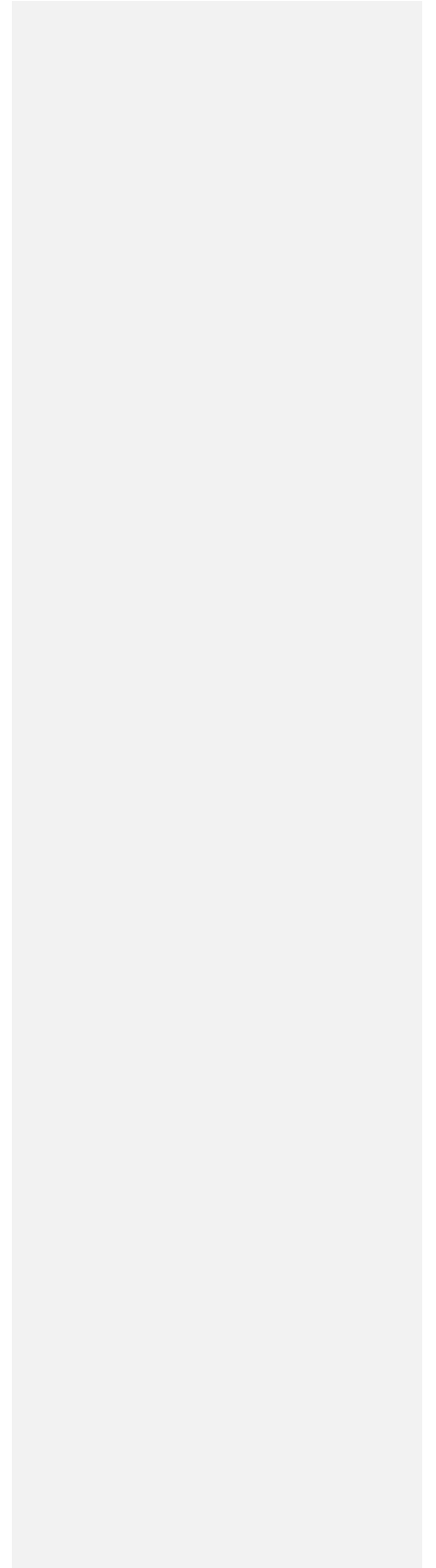
23 **Abstract**

24 Top-down estimates of the spatiotemporal variations in emissions and uptake of CO<sub>2</sub> will benefit  
25 from the increasing measurement density brought by recent and future additions to the suite of in  
26 situ and remote CO<sub>2</sub> measurement platforms. In particular, the planned NASA Active Sensing of  
27 CO<sub>2</sub> Emissions over Nights, Days, and Seasons (ASCENDS) satellite mission will provide  
28 greater coverage in cloudy regions, at high latitudes, and at night than passive satellite systems,  
29 as well as high precision and accuracy. In a novel approach to quantifying the ability of satellite  
30 column measurements to constrain CO<sub>2</sub> fluxes, we use a portable library of footprints (surface  
31 influence functions) generated by the WRF-STILT Lagrangian transport model in a regional  
32 Bayesian synthesis inversion. The regional Lagrangian [particle dispersion model](#) framework is  
33 well suited to make use of ASCENDS observations to constrain fluxes at high resolution, in this  
34 case at 1° latitude x 1° longitude and weekly for North America. We consider random  
35 measurement errors only, modeled as a function of mission and instrument design specifications  
36 along with realistic atmospheric and surface conditions. We find that the ASCENDS  
37 observations could potentially reduce flux uncertainties substantially at biome and finer scales.  
38 At the [1° x 1°-grid scale and](#) weekly [resolution-scale](#), the largest uncertainty reductions, on the  
39 order of 50%, occur where and when there is good coverage by observations with low  
40 measurement errors and the a priori uncertainties are large. Uncertainty reductions are smaller  
41 for a 1.57 μm candidate wavelength than for a 2.05 μm wavelength, and are smaller for the  
42 higher of the two measurement error levels that we consider (1.0 ppm vs. 0.5 ppm clear-sky error  
43 at Railroad Valley, Nevada). Uncertainty reductions at the annual, biome scale range from ~40%  
44 to ~75% across our four instrument design cases, and from ~65% to ~85% for the continent as a  
45 whole. [Tests suggest that the quantitative results are moderately sensitive to assumptions](#)

46 ~~regarding a priori uncertainties and boundary conditions. Our uncertainty reductions at various~~  
47 ~~scales are substantially smaller than those from a global ASCENDS inversion on a coarser grid,~~  
48 ~~demonstrating how quantitative results can depend on inversion methodology.~~ The a posteriori  
49 flux uncertainties we obtain, ranging from 0.01 to 0.06 Pg C yr<sup>-1</sup> across the biomes, would meet  
50 requirements for improved understanding of long-term carbon sinks suggested by a previous  
51 study.

52

53





54 **1. Introduction**

55 Quantification of surface fluxes of CO<sub>2</sub> and other greenhouse gases (GHG) over a range  
56 of spatial and temporal scales is of critical importance for understanding the processes that drive  
57 source/sink variability and climate-biogeochemistry feedbacks. The need to monitor GHG  
58 fluxes also follows from climate policy initiatives such as the Kyoto Protocol and possible  
59 follow-on agreements, along with their implementation (e.g., emissions trading and treaty  
60 verification). While direct “bottom-up” (inventory) approaches are considered accurate to within  
61 10% in the annual mean for fossil fuel CO<sub>2</sub> emissions in North America [*Gurney et al.*, 2009],  
62 “top-down” (inverse) methods are the tool of choice to infer CO<sub>2</sub> sources and sinks from the  
63 terrestrial biosphere and oceans on a range of scales [*Peters et al.*, 2007]. In the top-down  
64 approach, fluxes are inferred from atmospheric CO<sub>2</sub> measurements by means of an atmospheric  
65 transport model linking the measurements to fluxes upwind. The availability of abundant and  
66 accurate measurements and realistic transport models is key to the success of this approach [e.g.  
67 Enting et al., 1995]. Consequently, large investments have been made in establishing reliable  
68 measurement networks, including in situ measurements of CO<sub>2</sub> concentrations from the surface,  
69 towers, and aircraft (e.g. the NOAA ESRL Carbon Cycle Cooperative Global Air Sampling  
70 Network [*Dlugokencky et al.*, 2013], and the Earth Networks Greenhouse Gas Network,  
71 <http://ghg.earthnetworks.com/>), and satellite missions dedicated to measurement of CO<sub>2</sub> column  
72 amounts. The last include the Greenhouse gases Observing SATellite (GOSAT) launched in  
73 ~~January, 2009~~ [*Yokota et al.*, 2009], the Orbiting Carbon Observatory 2 (OCO-2) ~~to be~~-launched  
74 in 2014 [*Crisp et al.*, 2008; *Eldering et al.*, 2012], and the planned Active Sensing of CO<sub>2</sub>  
75 Emissions over Nights, Days, and Seasons (ASCENDS) mission recommended by the U.S.  
76 National Academy of Sciences Decadal Survey [*NRC*, 2007].

77           The objective of our study is to quantify the ability of ASCENDS column measurements  
78 to constrain CO<sub>2</sub> fluxes top-down at relatively high resolution. The ASCENDS active  
79 measurement concept offers unique capabilities compared with passive satellite systems that rely  
80 on thermal emission or reflected sunlight [Kawa et al., 2010]. These capabilities will enhance  
81 spatial and temporal coverage while providing high precision and accuracy. ASCENDS will  
82 extend coverage through its ability to sample in small cloud gaps and through thin clouds  
83 without interference. In addition, since a lidar-based system does not require the presence of the  
84 sun, it allows for observations of high-latitude regions during winter. Measurements can be  
85 made both night and day, thereby reducing sampling bias due to (and potentially providing  
86 constraints on) diurnal variations in CO<sub>2</sub> fluxes driven by ecosystem respiration and primary  
87 production.

88           Global studies of the impact of satellite measurements on top-down estimates of CO<sub>2</sub>  
89 fluxes, beginning with the study of *Rayner and O'Brien* [2001], have established the benefit of  
90 using satellite measurements for constraining CO<sub>2</sub> fluxes at a precision level similar to or better  
91 than that provided by existing in situ networks. At present, these approaches estimate the  
92 reduction of flux uncertainties stemming from the availability of satellite data using an inverse  
93 solution for relatively coarse grid boxes or regions at weekly to monthly resolution [e.g.  
94 Houweling et al., 2004; Chevallier et al., 2007; Feng et al., 2009; Baker et al., 2010; Kaminski et  
95 al., 2010; Hungerschoefer et al., 2010; Basu et al., 2013; [Deng et al., 2014](#)]. The present study  
96 extends these global studies to the regional scale using simulated ASCENDS data. Regional  
97 trace gas inversions are well-suited for making use of high-density satellite observations to  
98 constrain fluxes at fine scales. Regional transport models are less computationally expensive to  
99 run than global transport models for a given resolution, so it is more tractable to run a regional

100 model at high resolution. The more precise determination of source-receptor relationships  
101 allows one to solve for fluxes at a finer resolution. This reduces potential “aggregation error”  
102 resulting from assuming fixed fine-scale flux patterns when optimizing scaling factors on a  
103 coarser scale [Kaminski et al., 2001; Engelen et al., 2002; Gerbig et al., 2003; [Bocquet et al.,](#)  
104 [2011](#)].

105 We use a novel approach for our inversions that facilitates high-resolution evaluation of  
106 satellite column measurements. The approach relies on a Lagrangian, ~~(or airmass-following,)~~  
107 transport model ~~(as opposed to an Eulerian, or fixed-frame-of-reference, model)~~, run backward  
108 in time from the observation points (receptors) using ensembles of particles, to generate  
109 footprints describing the sensitivity of satellite CO<sub>2</sub> measurements to surface fluxes in upwind  
110 regions. ~~Lagrangian particle dispersion models~~~~This approach~~ enables more precise simulation of  
111 transport in the near field than ~~gridded transport models~~~~running source pulses through an~~  
112 ~~Eulerian (with fixed frame of reference) transport model~~, since, in the former, ~~particle locations~~  
113 ~~are not restricted to a grid and~~ meteorological fields are interpolated to the subgrid-scale  
114 locations ~~of particles~~. Thus, filamentation processes, for example, can be resolved [Lin et al.,  
115 2003], ~~artificial diffusion over grid cells is avoided~~, and representation errors [Pillai et al., 2010]  
116 are minimized. The Lagrangian approach, implemented in the backward (receptor-oriented)  
117 mode, offers a natural way of calculating the adjoint of the atmospheric transport model. The  
118 utility of Lagrangian particle dispersion models is well established for regional trace gas flux  
119 inversions involving in situ observations [e.g. Gerbig et al., 2003; Lin et al., 2004; Kort et al.,  
120 2008, 2010; Zhao et al., 2009; Schuh et al., 2010; Göckede et al., 2010a; [Brioude et al., 2011,](#)  
121 [2012, 2013;](#) Gourdji et al., 2012; Miller et al., 2012, 2013; McKain et al., 2012; Lauvaux et al.,  
122 2012]. A convenient feature of Lagrangian footprints is their portability—they can be shared

123 with other groups and readily applied to different flux models, inversion approaches, and  
124 molecular species, thus enabling comparisons based on a common modeling component. In  
125 addition, footprints for different measurement platforms can be merged easily in an inversion.

126 In this observing system simulation experiment (OSSE), we utilize the Stochastic Time-  
127 Inverted Lagrangian Transport (STILT) particle dispersion model [Lin et al., 2003] driven by  
128 meteorological fields from the Weather Research and Forecasting (WRF) model [Skamarock and  
129 Klemm, 2008] in a domain encompassing North America, in a Bayesian inversion. The WRF-  
130 STILT [Nehrkorn et al., 2010] footprints are used to compute weekly flux uncertainties over a 1°  
131 latitude x 1° longitude grid. This study focuses on land-based biospheric fluxes. We report  
132 results based on realistic sampling and observation errors for [a set of ASCENDS instrument](#)  
133 [designs](#) and other input data fields for year 2007. Section 2 provides details on our inputs and  
134 inversion methods, and presents examples of observation uncertainties, a priori flux  
135 uncertainties, and WRF-STILT footprint maps. Section 3 presents posterior flux uncertainty  
136 results at various spatial and temporal scales, as well as comparisons with other studies,  
137 ~~including preliminary results from a companion global ASCENDS OSSE~~. Section 4 discusses  
138 target and threshold requirements for instrument design parameters with respect to addressing  
139 key scientific questions. It also discusses [sensitivity to](#) additional sources of uncertainty and  
140 limitations of our analysis, as well as other considerations regarding ASCENDS. Section 5  
141 contains concluding remarks.

142

143

## 144 2. Methods

### 145 2.1. Inversion Approach

Formatted: Indent: First line: 0.5"

146 We use a Bayesian synthesis inversion method, which optimizes the agreement between  
147 model and observed CO<sub>2</sub> concentrations and a priori and a posteriori flux estimates in a least-  
148 squares manner [e.g. Enting et al., 1995]. Since we focus on ~~random uncertainty error~~ levels in  
149 ~~estimating-constraining~~ the ~~constraint-on~~ fluxes ~~that-using~~ ASCENDS observations ~~will provide~~,  
150 we did not perform a full inversion and computed only the a posteriori flux error covariance  
151 associated with the inversion solution. The a posteriori flux error covariance matrix is given by

$$152 \hat{\mathbf{S}} = (\mathbf{K}^T \mathbf{S}_e^{-1} \mathbf{K} + \mathbf{S}_a^{-1})^{-1}, \quad (1)$$

where

$\mathbf{K}$  is the Jacobian matrix describing the sensitivity of concentrations to changes in the state vector  
153 elements (in this case, fluxes)

$\mathbf{S}_e$  is the observation error covariance matrix

$\mathbf{S}_a$  is the a priori flux error covariance matrix.

154 We directly solve for  $\hat{\mathbf{S}}$ , the square roots of the diagonal elements of which provide the estimates  
155 of the a posteriori flux uncertainties.

156 We solve for flux uncertainties in each land cell on a 1° x 1° grid across North America  
157 (from 10°N to 70°N and from 170°W to 50°W). The time span is 5 weeks in each of the 4  
158 seasons in 2007 (the first 4 weeks of January, April, July, and October plus the week preceding  
159 each of those months). We focus on weekly flux resolution in this study, rather than daily or  
160 higher resolution, for computational efficiency. In addition, the Decadal Survey called for a  
161 satellite mission that can constrain carbon cycle fluxes at weekly resolution on 1° grids [NRC,  
162 2007]. The ASCENDS observations would likely also provide significant constraints on fluxes  
163 at higher resolutions such as daily, as suggested by test inversions not reported here.

164 We solve Eq. (1) using the standard matrix inversion function in the Interactive Data  
165 Language (IDL) software package. We verified the solution using the alternative singular value

166 decomposition approach [Rayner et al., 1999], again in IDL. Given the large dimensions of the  
167 matrices-- more than 15,000 10-s average observations each month and 13,205 weekly flux  
168 elements over each 5-week period, the procedure requires large amounts of computer memory  
169 but a modest amount of processing time--several hours per monthly inversion on the NASA  
170 Center for Climate Simulation high-performance computing system.

171

## 172 2.2. Observational Sampling and Simulated Measurement Uncertainties

173 We consider candidate lidar wavelengths near 1.57  $\mu\text{m}$  and 2.05  $\mu\text{m}$  [Caron and Durand,  
174 2009]. These have peak sensitivities in the mid- and lower troposphere, respectively (Figure 1).  
175 Other candidate wavelengths with different vertical sensitivities and error characteristics are  
176 possible and could be assessed with the same inversion methodology. We derive the  
177 temporal/spatial sampling and random error characteristics for ASCENDS pseudo-data based on  
178 real cloud/aerosol and surface backscatter conditions for year 2007 in a method similar to that of  
179 Kawa et al. [2010]. Observation locations are taken from Cloud-Aerosol Lidar and Infrared  
180 Pathfinder Satellite Observation (CALIPSO) satellite orbit tracks. We use only locations that fall  
181 within the domain used in the WRF runs (Section 2.4), excluding those within 400 km of the  
182 boundaries to provide adequate WRF coverage to simulate back trajectory calculations inside the  
183 domain (Figure 2). The errors are calculated as a function of CALIPSO optical depth  
184 (OD) measured by CALIPSO data, together with and surface backscatter calculated from  
185 Moderate Resolution Imaging Spectroradiometer (MODIS) satellite reflectance over land or glint  
186 backscatter, calculated using 10-m analyzed wind speeds [Hu et al., 2008] interpolated to the  
187 sample locations, over ocean. Samples with total column cloud plus aerosol OD > 0.7 are  
188 rejected. For each wavelength case, the measurement errors at each location are scaled to two

189 possible performance levels: 0.5 ppm and 1.0 ppm error (10 s average) under clear-sky  
190 conditions (cloud/aerosol OD = 0) with for a reflectivity equal to that found at a reference site,  
191 Railroad Valley (RRV), Nevada. The errors for each 5 km (0.74 s) individual CALIPSO  
192 observation point are aggregated over 10-s (67 km) intervals to increase signal-to-noise for the  
193 pseudo-data, using the formula  $\sigma(10s) = \sqrt{\frac{\sum_{i=1}^N \sigma(5km)_i^2}{N^2}}$ , where N is the number of valid 5 km  
194 observations across the 10-s span. Such a 10-s, conditionally-sampled measurement is expected  
195 to represent the basic ASCENDS CO<sub>2</sub> data granule. The uncertainties in the series of 10-s  
196 pseudo-data are assumed to be uncorrelated, i.e. the observation error covariance matrix  $S_e$  is  
197 diagonal.

198 Examples of the coverage of ASCENDS observations available for analysis and their  
199 associated uncertainties (for a reference uncertainty at RRV of 0.5 ppm) are shown in Figure 2  
200 over seven-day periods in January and July for the two candidate wavelengths. ASCENDS  
201 provides dense coverage over the domain with few large gaps, especially in July. A large  
202 majority of the 10 second-average observations have uncertainties of < 2 ppm in all four cases  
203 except for 2.05  $\mu\text{m}$  in January. The uncertainties are especially small over land areas, which is  
204 helpful for constraining terrestrial fluxes. The uncertainties are generally larger for 2.05  $\mu\text{m}$  than  
205 for 1.57  $\mu\text{m}$  (by a factor of 1-1.6 over snow-free land and a factor of 1.6-1.8 over snow-/ice-  
206 covered areas) except in ice-free oceanic areas, where the uncertainties are similar (Figure 2e and  
207 2f).

208

### 209 2.3. A Priori Flux Uncertainties

210 We derived a priori flux uncertainties at 1° x 1° resolution from the variability of net  
211 ecosystem exchange (NEE) in the Carnegie-Ames-Stanford-Approach (CASA) biogeochemical

212 model coupled to version 3 of the Global Fire Emissions Database (GFED3) [Randerson et al.,  
213 1996; van der Werf et al., 2006; 2010]. CASA-GFED is driven with meteorological data from  
214 the Modern-Era Retrospective Analysis for Research and Applications (MERRA) [Rienecker et  
215 al., 2011]. In the version of CASA used here, a sink of  $\sim 100 \text{ Tg C yr}^{-1}$  is induced by crop  
216 harvest in the U.S. Midwest that is prescribed based on National Agriculture Statistics Service  
217 data on crop area and harvest. We neglected uncertainties in fossil fuel emissions, assuming like  
218 most previous inversion studies that those emissions are relatively well known. We ignored  
219 oceanic fluxes as well for this study, since their uncertainties are also relatively small [e.g. Baker  
220 et al., 2010].

221 The a priori flux uncertainties were specifically derived from the standard deviations of  
222 daily mean CASA-GFED NEE over each month in 2007, divided by  $\sqrt{7}$  to scale approximately  
223 to weekly uncertainties. This approach assumes that the more variable the model fluxes are in a  
224 particular grid cell and month, the larger the errors tend to be; the same reasoning has been  
225 applied in previous inversion studies to the estimation of model-data mismatch errors [e.g. Wang  
226 et al., 2008]. We enlarged the resulting uncertainties uniformly by a factor of 4 to approximate  
227 the magnitude of those used in the global ASCENDS OSSE described in [Section 3.2](#) of this  
228 paper; these are, in turn, essentially the same as the standard ones of Baker et al. [2010], based  
229 on differences between two sets of bottom-up flux estimates. In addition to allowing for better  
230 comparison of the two OSSEs, the enlargement by a factor of 4 is consistent with suggestions by  
231 biospheric model intercomparisons that the true flux uncertainty is greater than that based on a  
232 single model's variability [Huntzinger et al., 2012].

233 Off-diagonal elements of the a priori flux error covariance matrix are filled using spatial  
234 and temporal error correlations derived from an isotropic exponential decay model with month-



235 specific correlation lengths (Table 1) estimated from ground-based and aircraft CO<sub>2</sub> data in a  
236 North America regional inversion by Gourdjı et al. [2012]. Although these correlation lengths  
237 are not strictly applicable to our study, which has a different setup from that in the geostatistical  
238 inverse modeling system of Gourdjı et al., they are nonetheless reasonable estimates in general  
239 for the purposes of this study. Note that Gourdjı et al. used a 3-hourly flux resolution, so the  
240 temporal correlation lengths may be too short for the coarser weekly resolution of our study.  
241 Chevallier et al. [2012] show that aggregation of fluxes to coarser scales increases the error  
242 correlation length. The analysis by Chevallier et al. [2012] using global flux tower data found a  
243 weekly-scale temporal error correlation length of 36 days, longer than the values we use. They  
244 found a spatial correlation length of less than 100 km at the site scale (~1 km), increasing to 500  
245 km at a 300 km-grid scale; our correlation lengths (100 km-grid) mostly fall within that range.  
246 In a test, we used alternative values for the spatiotemporal correlation lengths derived from the  
247 Chevallier et al. study, and found that the inversion results are moderately sensitive (Section  
248 [4.3.2](#)).

249 Our CASA-GFED-based a priori flux uncertainties, scaled to approximate the values  
250 used by Baker *et al.* [2010], are shown in Figure 3. The largest uncertainties occur generally  
251 where the absolute value of NEE is highest, e.g., in the “Corn Belt” of the U.S. in summer. The  
252 spatial and seasonal variations exhibit similarities to those of Baker et al.

253

#### 254 2.4. WRF-STILT Model, Footprints, and Jacobians

255 The STILT Lagrangian model, driven by WRF meteorological fields, has features,  
256 including a realistic treatment of convective fluxes and mass conservation properties, that are  
257 important for accurate top-down estimates of GHG fluxes that rely on small gradients in the

258 measured concentrations [*Nehrkorn et al.*, 2010]. In the present application of STILT  
259 ([www.stilt-model.org](http://www.stilt-model.org), revision 640), hourly output from WRF version 2.2 is used to provide the  
260 transport fields at a horizontal resolution of 40 km with 31 eta levels in the vertical, over a North  
261 American domain (Figure 2a). Meteorological fields from the North American Regional  
262 Reanalysis (NARR) at 32-km resolution are used to provide initial and boundary conditions for  
263 the WRF runs. To prevent drift of the WRF simulations from the analyses, the meteorological  
264 fields (horizontal winds, temperature, and water vapor at all levels) are nudged to the NARR  
265 analysis every 3 hours with a 1-hour relaxation time and are reinitialized every 24 hours (at 00  
266 UTC). Simulations are run out for 30 hours, but only hours 7-30 from each simulation are used  
267 to avoid spin-up effects during the first 6 hours. The WRF physics options used here are the  
268 same as those described by *Nehrkorn et al.* [2010].

269         A footprint quantitatively describes how much surface fluxes originating in upwind  
270 regions contribute to the total mixing ratio at a particular measurement location; it has units of  
271 mixing ratio per unit flux. This is to be distinguished from a satellite footprint, the area of earth  
272 reflecting the lidar signal. In the current application, footprints are computed for each 5-km  
273 simulated observation that passes the cloud/aerosol filter in January, April, July, and October  
274 2007 at 3-hour intervals back to 10 days prior to the observation time. Separate footprint maps  
275 have been computed for 15 receptor positions above ground level for the purpose of vertically  
276 convolving with the lidar weighting functions and producing one weighted-average footprint per  
277 measurement. (The receptors are spaced 1 km apart in the vertical from 0.5 to 14.5 km AGL.)  
278 This procedure results in ~90,000 footprint calculations per day, placing stringent demands on  
279 our computational approach. In this study, STILT simulates the release of an ensemble of 500  
280 particles at each receptor in the column.

281 It is important to note that although a footprint is defined for each of the 15 vertical  
282 levels, the footprint expresses the sensitivity of the mixing ratio measured at the receptor point  
283 located at that vertical level to the surface fluxes upwind, not the fluxes upwind at the same  
284 level. So intuitively, the footprints defined for receptor points located at high altitudes (e.g. 12.5,  
285 13.5, 14.5 km) are often zero, indicating that a receptor at that upper level is not influenced by  
286 surface fluxes inside the domain (within the 10 day span examined here). Conversely, receptor  
287 points located at the lowest levels (e.g. 0.5, 1.5, 2.5 km) tend to have large footprints (with  
288 values of the order of  $10^{-3}$  ppm/( $\mu\text{mol}/\text{m}^2/\text{s}$ ) or higher), being most influenced by nearby surface  
289 fluxes.

290 Figure 4 shows the vertically-weighted footprints of a selected column measurement  
291 location (in southern Canada) over 10 days for the 1.57 and 2.05  $\mu\text{m}$  wavelengths. Non-zero  
292 footprints occur wherever air observed at the receptor site has been in contact with the surface  
293 within the past 10 days. Patterns of vertical and horizontal atmospheric motion explain the  
294 somewhat unexpected spatial patterns of the footprints in this particular example, with very high  
295 values occurring at a significant distance upwind of the receptor (in the vicinity of Texas and  
296 Oklahoma) as well as immediately upwind. Vertical mixing lifts the signature of surface fluxes  
297 to higher levels, so that it can be detected by receptors at multiple levels, resulting in a higher  
298 value for the vertically-convolved footprint, while slower winds in a particular area, such as  
299 Texas and Oklahoma, can result in a larger time-integrated impact of fluxes on the observation.  
300 The footprint values are larger for 2.05  $\mu\text{m}$  due to the higher sensitivity of that measurement near  
301 the surface, as previously discussed.

302 To construct the Jacobians,  $\mathbf{K}$ , that enter Eq. (1), we averaged the footprints of all the 5-  
303 km receptor locations within a given 10-s interval averaging period along the satellite track,

304 including only the land cells. We arranged the averaged footprints in a two-dimensional  
305 Jacobian, running across flux time intervals and grid cells in one direction and across  
306 observations in the other. (The 3-hour flux intervals associated with each transport run are  
307 defined relative to fixed UTC times and not relative to the observation times.) We then  
308 aggregated the Jacobian elements to the final flux resolution, e.g., weekly. For any particular  
309 month, we solved only for fluxes occurring in the week prior to the beginning of the month and  
310 in the first 4 weeks of that month.

311 Figure 5 shows the overall influence of the surface fluxes on the observations during each  
312 month (i.e. the average weekly Jacobian values for the  $1.57 \mu\text{m}$  weighting function). Values  
313 tend to decrease from west to east, reflecting the general westerly wind direction, which  
314 transports  $\text{CO}_2$  influences out of the domain more quickly for fluxes occurring closer to the  
315 eastern edge than for those farther west. Values also tend to decrease towards the north and  
316 northwest and in the southernmost part of the continent: these areas lie close to the edges of the  
317 domain shown in Figure 2a. Areas with smaller average footprint values are generally not as  
318 well constrained by the observations, as will be discussed later in this paper; thus, our domain  
319 boundaries artificially limit flux constraints in certain parts of the continent. Previous regional  
320 inversion studies may not have highlighted this issue because they used ground-based  
321 observations, whose sensitivities are more confined to near-field fluxes than those of satellite  
322 column measurements. We will quantify the impact of the boundaries on average footprint  
323 gradients in future work, providing guidance for future studies on optimal sizes and shapes of  
324 domains (e.g. shifted eastward) for avoiding large gradients while controlling computational  
325 cost.

326 Footprint values are largest in summer, again due to horizontal and vertical motions—  
327 winds during this season are relatively light and allow the fluxes to stay inside the domain for a  
328 long time, maximizing their integrated influence on observations in the domain, and vertical  
329 mixing across the deep boundary layer brings particles over a large portion of the column into  
330 contact with the surface.

331 Although WRF-STILT provides the capability to generate and optimize boundary  
332 condition influences on observed concentrations, this was not available at the time of this study  
333 and, consequently, we neglect uncertainties in the influence of boundary conditions in ~~this-our~~  
334 ~~standard inversion analysis~~ (discussed further in Section 4.24). Similarly, we neglect  
335 uncertainties due to the influence of North American fluxes occurring more than 10 days before  
336 a particular observation. Note that fluxes are often transported out of the domain within 10 days,  
337 so that these fluxes can only influence the observations via the boundary conditions.

338

339

### 340 3. Results

341 In the following, we present results for four cases involving different combinations of  
342 measurement wavelength and baseline error level: 1.57  $\mu\text{m}$  and 0.5 ppm RRV error (Case 1),  
343 1.57  $\mu\text{m}$  and 1.0 ppm (Case 2), 2.05  $\mu\text{m}$  and 0.5 ppm (Case 3), and 2.05  $\mu\text{m}$  and 1.0 ppm (Case  
344 4).

345

#### 346 3.1. A Posteriori Flux Uncertainties at the Grid Level

347 A posteriori uncertainties (Figure 6) are smaller than the a priori values (Figure 3), an  
348 expected result of the incorporation of observational information. The reduction in uncertainty is

349 often larger in areas that have higher a priori uncertainties, as can be seen more clearly in the  
350 maps of percentage reduction in uncertainty in Figure 7. Uncertainty reductions are relatively  
351 large year-round in places such as southern Mexico, ~~adjacent parts of Central America,~~ and the  
352 Pacific Northwest of the U.S.; in April and October in the southeastern U.S.; and in July in the  
353 U.S. Midwest, ~~southern Quebec,~~ areas with forest fire emissions in central Canada (appearing as  
354 hot spots of uncertainty reduction), and Alaska and western Canada. A priori uncertainties are  
355 relatively high in these areas, so that there is more room for observations to tighten the  
356 constraint. In contrast, The dependence of uncertainty reductions on the assumed priors can be  
357 ~~understood thus:~~ where a priori uncertainties are already small, observations are not able to  
358 provide a much tighter constraint, ~~while in areas where a priori uncertainties are large, there is~~  
359 ~~more room for observations to tighten the constraint.~~

360 Of course, ~~t~~he uncertainty reductions are not dependent simply on the prior  
361 uncertainties ~~though~~. For example, the highest uncertainty reductions, up to 50%, occur in  
362 southern Mexico in October, where a priori uncertainties are not especially large. The high  
363 uncertainty reductions here can be explained by the large Jacobian values (Figure 5) combined  
364 with the low uncertainties of nearby observations (not shown). (Although a priori uncertainties  
365 and Jacobian values in July in this area are similar to those in October, observation uncertainties  
366 are higher, resulting in lower uncertainty reductions.) ~~In general,~~ The tendency of uncertainty  
367 reductions ~~tend~~ to be higher where average Jacobian values are larger; can also be seen in  
368 ~~observe~~ the similarity of the spatial patterns in the January maps in Figures 5a and 7a, for  
369 example. As described in Section 2.4, fluxes in western and central areas of the continent are  
370 captured by more observations in the domain than fluxes in the east and close to the other edges;  
371 thus, the former can be better constrained in this inversion.

372 | ~~Another feature is that i~~n July, the largest uncertainty reductions occur in northern  
373 | Alaska and northwestern Canada, which have much smaller a priori uncertainties than places  
374 | such as the Midwest. This is an effect of the smaller grid cells at higher latitudes: the a priori  
375 | errors are correlated over larger numbers of cells at these latitudes given the spatially uniform  
376 | correlation lengths we specify, so that the average flux over each cell is more tightly constrained  
377 | than that for an otherwise comparable cell at lower latitudes. This is a less important issue when  
378 | results are aggregated to the larger scales dealt with in later sections of this paper.

379 | Uncertainty reductions are smallest in January, for several reasons: 1) a priori flux  
380 | uncertainties are smallest during the dormant season, 2) observation errors are largest in winter  
381 | due to the low reflectance of snow and ice cover at the measurement wavelengths, and 3) there is  
382 | fast dispersion of fluxes in winter by strong winds, transporting fluxes out of the domain and out  
383 | of detection by observations in the domain and thus reducing the average Jacobian values in  
384 | January relative to the other months (Figure 5). The ratio of the average of the Jacobian  
385 | elements over the domain for January to that for July is 0.51 for the 1.57  $\mu\text{m}$  wavelength.

386 | Inversions for the 2.05  $\mu\text{m}$  wavelength, with its higher sensitivity near the surface, result  
387 | in greater uncertainty reduction, despite the larger observation errors over land (Figure 8c vs. 8a,  
388 | and 8d vs. 8b). Inversions assuming 1.0 ppm instead of 0.5 ppm error at RRV result in less  
389 | uncertainty reduction (Figure 8b vs. 8a, and 8d vs. 8c) as expected, with maximum uncertainty  
390 | reduction of  $\sim 30\%$  vs.  $\sim 40\%$ , for 1.57  $\mu\text{m}$ . These cases are compared further in the section  
391 | below on biome-aggregated results.

392 | ~~The inversion results are sensitive to the assumed a priori error correlation lengths, with~~  
393 | ~~longer correlation lengths leading to more smooth uncertainty reduction patterns and larger~~  
394 | ~~uncertainty reductions. The reason for this is that longer a priori error correlation lengths result~~

395 in fewer “unknowns” to be constrained by the observations. Rodgers [2000] shows that the  
396 inclusion of a priori correlations can result in more “degrees of freedom for signal,” i.e. more  
397 information provided by the measurements on the unknowns. We carried out a test with  
398 alternative values for the correlation lengths derived from the study by Chevallier et al. [2012] —  
399 a shorter spatial correlation length of 200 km and a longer temporal correlation length of 35  
400 days, for all months. (We estimated these values from Figure 5a and b of Chevallier et al. for the  
401 100 km and 7-day aggregation of our inversion.) The resulting uncertainty reductions are  
402 smaller everywhere than those in our standard inversion at the grid scale, with values of up to  
403 40% in July and up to 15% in January for Case 1 (compared to 45% and 25%, respectively, in  
404 the standard inversion). Apparently, the decrease in the spatial correlation length relative to the  
405 standard inversion has a larger effect than the increase in the temporal correlation length. We  
406 conclude that our inversion results vary moderately given two reasonable sets of estimates for the  
407 a priori spatiotemporal error correlation lengths.

### 409 3.2. Comparison with Global Inversion

410 — We compare our regional OSSE results with those from a companion global OSSE to  
411 assess effects of methodological differences. The global OSSE uses the same ASCENDS dataset  
412 sampling and underlying observation error model as the regional OSSE. Among the primary  
413 differences are the global domain of the analysis and the coarser spatial resolution of the  
414 transport and flux solution,  $4.5^\circ$  latitude  $\times$   $6^\circ$  longitude. Other differences include the  
415 mathematical technique of the inversion (variational data assimilation, as in an earlier study  
416 [Baker et al., 2010]), the Eulerian transport model, the spatial patterns of the a priori flux  
417 uncertainties (the overall magnitudes are not different, as described in Section 2.3), and the



418 assumption of zero a priori correlation among fluxes (which can be justified by the coarser  
419 spatial scale). Comparison of our inversion results with results from the global study yields  
420 insight into the effect of inversion resolution on estimated flux uncertainties.  
421 To aggregate our flux uncertainties to  $4.5^\circ \times 6^\circ$  resolution (in units of  $\mu\text{mol m}^{-2}\text{s}^{-1}$ ) for  
422 comparison with the global inversion, we computed the variance of the average of the  $1^\circ \times 1^\circ$   
423 land fluxes within each coarse grid cell, accounting for the error correlations between the fine-  
424 scale cells and accounting for fractional overlap of some of the  $1^\circ \times 1^\circ$  cells with a  $4.5^\circ \times 6^\circ$  cell.  
425 Aggregating our a priori and a posteriori uncertainties in this manner, we find that our fractional  
426 uncertainty reductions over the 4 months are substantially smaller overall than those of the global  
427 inversion (Figure 9). The differences in spatial distribution can be attributed in part to the  
428 different a priori uncertainty patterns. Reductions greater than 55% cover large areas of North  
429 America in the global inversion, reaching values of over 75%, whereas only a few  $4.5^\circ \times 6^\circ$  cells  
430 exhibit values greater than 55% in the regional inversion. Note that we are not comparing  
431 exactly the same quantity, as the variational inversion method does not directly compute a full a  
432 posteriori error covariance matrix; rather, it uses (estimate – truth) statistics as a proxy for  
433 uncertainty, which is accurate for a sufficiently large sample [Baker et al., 2010]. One possible  
434 reason for the difference in results is that information from the observations is used to optimize  
435 the fine scale patterns in addition to the coarse scale magnitudes in our inversion, in contrast to  
436 the global inversion in which a flat spatial distribution of flux is assumed inside each coarse grid  
437 box, providing an additional constraint on the fluxes. Thus, in our inversion, less information is  
438 available to reduce the uncertainties of the coarse scale magnitudes, causing our uncertainty  
439 reductions to be smaller than those of the global inversion when compared at the same scale.  
440 (Note however that our imposing of a priori flux error correlations provides an additional

Formatted: Indent: First line: 0"

441 ~~constraint on fluxes and reduces the difference in effective flux resolution between the two~~  
442 ~~studies.) On the other hand, the coarser global inversion is affected by larger aggregation errors~~  
443 ~~[Kaminski et al., 2001; Engelen et al., 2002; Gerbig et al., 2003], which are not accounted for in~~  
444 ~~the uncertainty reduction values. Another factor that likely contributes to the larger uncertainty~~  
445 ~~reductions in the global inversion is that it allows fluxes to be constrained by observations both~~  
446 ~~outside and inside a particular region. This can be especially important for fluxes close to the~~  
447 ~~regional edges, as was discussed in Section 3.1. We do not attempt to quantify the individual~~  
448 ~~impacts of the two main methodological differences or the various other differences.~~

### 450 3.23. Results Aggregated to Biomes and Continent, and Compared with Other Inversion 451 Systems

452 For assessing large-scale changes in carbon sources and sinks, it is useful to aggregate  
453 high-resolution results to biomes and the entire continent, and to seasons and years. We use the  
454 biome definitions in Figure 9 taken from Olson et al. [2001] with modifications by Gourdj et al.  
455 [2012]. ~~To aggregate the flux uncertainties, we summed up the variances within each biome and~~  
456 ~~over each month and then the year (in units of  $(\text{Pg C yr}^{-1})^2$ ) as well as the error covariances~~  
457 ~~between grid cells and weeks. We used a similar approach for aggregating our results here to the~~  
458 ~~one we used to aggregate results to a coarser grid (Section 3.2).~~

459 ~~We compare our results with those from two other inversion systems: a global inversion~~  
460 ~~using ASCENDS observations (companion study to this one), and a North America regional~~  
461 ~~inversion using the same WRF-STILT Lagrangian model as ours but with a network of ground-~~  
462 ~~based observation sites [Gourdj et al., 2012]. The global OSSE uses the same ASCENDS~~  
463 ~~dataset sampling and underlying observation error model as the regional OSSE. Among the~~

Formatted: Superscript

Formatted: Superscript

464 primary differences are the global domain of the analysis (and thus the use of observations  
465 outside of the N. American domain as well as inside) and the coarser spatial resolution of the  
466 transport and flux solution, 4.5° latitude x 6° longitude. Other differences include the  
467 mathematical technique of the inversion (variational data assimilation, as in an earlier study  
468 [Baker et al., 2010]), the Eulerian transport model (PCTM; Kawa et al. [2004]), the spatial  
469 patterns of the a priori flux uncertainties (the overall magnitudes are not different, as described in  
470 Section 2.3), the assumption of zero a priori error correlations, and the use of (estimate - truth)  
471 statistics as a proxy for flux uncertainty [Baker et al., 2010], given that the variational method  
472 does not directly compute a full a posteriori error covariance matrix. ~~In addition, we~~  
473 aggregated the global inversion results to the same biomes for comparison, summing the  
474 (estimate - truth) values and accounting for fractional biome coverage in each of the coarse grid  
475 cells. Gourdjji et al. used a set of ground-based and aircraft measurements and a geostatistical  
476 inverse model to solve for biospheric fluxes and their uncertainties at a 1° x 1°, 3-hourly  
477 resolution in 2004. We present these comparisons mainly to provide context for our results,  
478 rather than to quantitatively analyze effects of various methodological differences. ~~In addition,~~  
479 we aggregated the global inversion results to the same biomes for comparison, summing the  
480 (estimate - truth) values and accounting for fractional biome coverage in each of the coarse grid  
481 cells.

482       Uncertainty reductions are largest in July and smallest in January, at the continental scale  
483 (Table 2). The uncertainty reductions for the 1.57  $\mu\text{m}$  wavelength are on average 8% smaller  
484 than those for 2.05  $\mu\text{m}$ . The uncertainty reductions for the 1.57  $\mu\text{m}$  wavelength with 0.5 ppm  
485 error are larger than those for 2.05  $\mu\text{m}$  with 1.0 ppm error. The uncertainty reductions for 0.5  
486 ppm error are on average 16% larger than those for 1.0 ppm error. ~~(Note that there is no reason~~

487 ~~to expect direct proportionality between measurement uncertainties and a posteriori flux~~  
488 ~~uncertainties (Eq. 1), nor is there reason to expect proportionality between uncertainty reduction~~  
489 ~~and a posteriori uncertainty.) The uncertainty reduction for the inversion with alternative a priori~~  
490 ~~error correlation lengths, aggregated to the continent and month, is less than that for the standard~~  
491 ~~inversion for all months except July, for which the uncertainty reduction is marginally larger.~~  
492 ~~For July, the impact of the much longer temporal correlation length relative to the standard~~  
493 ~~inversion on the aggregated result more than offsets that of the slightly shorter spatial correlation~~  
494 ~~length. The annual uncertainty reduction for the alternative inversion is slightly larger than that~~  
495 ~~for the standard inversion, because of the disproportionate influence of July, with its large a~~  
496 ~~priori uncertainty.~~

497         At the annual, biome scale, our uncertainty reductions range from 50% for the desert  
498 biome (averaged across the cases) to 70% for the temperate grassland/shrubland biome (Figure  
499 10+c). The reductions scale with increasing a priori uncertainty (Figure 10+a) and observation  
500 quality and density, as before, and now also with biome area (Figure 10+d). We find a modest  
501 correlation between uncertainty reduction and area in the set of biomes here, with a linear  
502 correlation coefficient of 0.5. In addition, the uncertainty reduction is higher on the continental  
503 scale than on the biome scale. The a posteriori uncertainty increases with increasing area more  
504 slowly than does the a priori uncertainty since many of the a posteriori error covariance terms  
505 that are summed in the aggregation to biome are negative, whereas all of the a priori error  
506 covariance terms are positive or zero. This explains why uncertainty reduction tends to increase  
507 with increasing area.

508         Our a posteriori uncertainties range from 0.12 to 0.33 Pg C yr<sup>-1</sup> at the monthly,  
509 continental scale across all four cases (Table 2), from 0.04 to 0.08 Pg C yr<sup>-1</sup> at the annual,

510 continental scale (Figure 10a), and from 0.01 to 0.06 Pg C yr<sup>-1</sup> at the annual, biome scale  
511 (Figure 10a). To put these numbers into perspective, the estimated current global terrestrial  
512 sink is roughly 2.5 Pg C yr<sup>-1</sup> [Le Quéré et al., 2012]. Our uncertainties are generally similar to  
513 those from the North American regional inversion of Gourdji et al. [2012] (Figure 10a) and the  
514 global inversion (Figure 10b), a notable exception being the overall continental result of  
515 Gourdji et al. ~~Gourdji et al. used a set of ground-based and aircraft measurements and a  
516 geostatistical inverse model to solve for biospheric fluxes and their uncertainties at a 1° x 1°, 3-  
517 hourly resolution in 2004.~~ Our a posteriori uncertainty for N. America is small compared to  
518 Gourdji et al., likely because of the greater spatial coverage of ASCENDS as compared to the in  
519 situ network; some of the biomes are not well constrained by the in situ network (i.e. the ones for  
520 which Gourdji et al. did not report aggregated results). Note that the comparison is not totally  
521 consistent a precise one, given the methodological differences. The global inversion's method for  
522 estimating uncertainties based on (estimate - truth) statistics cannot provide an annual  
523 uncertainty estimate for the one-year inversion and produces somewhat noisy results for  
524 individual months. Therefore, to compare the regional and global inversions, we took the RMS  
525 of the four monthly uncertainties. ~~Our~~ The uncertainty reduction for our regional inversion is  
526 smaller than similar on average to that of the global inversion across ~~all~~ biomes and also for the  
527 continent as a whole for Case 1 (Figure 10c), with continent-level values of 78% and 72%,  
528 respectively. ~~despite~~ There are larger differences between the regional and global inversions for  
529 particular biomes. Although differences in prior uncertainty (Figure 10b) could possibly explain  
530 the differences in uncertainty reduction for some of the biomes (subtropical/tropical, eastern  
531 temperate, temperate coniferous, desert), they do not for the others (boreal, tundra, temperate  
532 grassland/shrubland), suggesting that prior uncertainties are not the only factor producing the

533 ~~spatial pattern in the comparison. the prior uncertainties being of similar magnitude on average~~  
534 ~~(Figure 11b). However, the continent-level uncertainty reductions are similar, at 78% and 83%,~~  
535 ~~respectively, suggesting that there are larger negative correlations in the posterior errors among~~  
536 ~~biomes in our analysis.~~

537

538

## 539 **4. Discussion**

### 540 4.1. Target and Threshold Requirements

541 We now discuss the implications of our analysis for the ASCENDS design.  
542 Hungershofer et al. [2010] suggested levels of posterior flux uncertainty on different  
543 spatiotemporal scales that global CO<sub>2</sub> measurement missions should strive for to allow for  
544 answering key carbon cycle science questions. In the following, we evaluate our results relative  
545 to those requirements, the only such specific guidelines for CO<sub>2</sub> satellite missions in the  
546 scientific literature.

547 Hungershofer et al. suggested that to determine where the global terrestrial C sink is  
548 occurring and whether C cycle feedbacks are occurring requires annual net carbon flux estimates  
549 with a precision better than 0.1 Pg C yr<sup>-1</sup> (threshold) or 0.02 Pg C yr<sup>-1</sup> (target) at a scale of 2000  
550 x 2000 km, similar to the biomes we consider. These precision levels are based on the range of  
551 estimated fluxes across various biomes. The proposed A-SCOPE active CO<sub>2</sub> measurement  
552 mission defined a similar target requirement—0.02 Pg C yr<sup>-1</sup> at a scale of 1000 x 1000 km  
553 [Ingmann et al., 2008]. According to our results (Figure 10a), all tested ASCENDS cases  
554 would meet the minimum threshold requirement across all biomes easily, with a posteriori  
555 uncertainties ranging from 0.01 to 0.06 Pg C yr<sup>-1</sup>. In addition, the two cases with 0.5 ppm error

556 would meet the more stringent target requirement for a majority of biomes, while the two cases  
557 with 1.0 ppm error would meet it for 3 out of 7 biomes. The meeting of the target requirement is  
558 a consequence of the information provided by the observations and not merely an effect of the  
559 specified a priori uncertainty, given that the a priori uncertainty is higher than the target level for  
560 all of the biomes with the exception of desert, the prior uncertainty for which is already at the  
561 target level. One measure of the contribution of the observations to meeting the target is shown  
562 in Figure 10e, which is a plot of the fractional uncertainty reduction necessary for different  
563 biomes to meet the target. The amounts are mostly greater than 50%, ranging up to 85% for  
564 eastern temperate.

566 4.2. Sensitivity Tests: Boundary Conditions, ~~Uncertainties~~ A Priori Uncertainties, and  
567 Correlation Lengths

568 A simplifying assumption in this analysis ~~our standard inversion~~ is the neglect of  
569 uncertainties in the boundary conditions (b.c.). It is especially important in a regional inversion  
570 (Eulerian or Lagrangian) to accurately account for the influence of lateral boundary inflow on  
571 concentrations within the domain [Göckede et al., 2010b; Lauvaux et al., 2012; Gourdji et al.,  
572 2012]. Because we neglect b.c. uncertainties, we essentially assume that all of the information  
573 in the ASCENDS observations can be applied to reducing regional flux uncertainties rather than  
574 the combination of b.c. and flux uncertainties. Thus, the amount of flux uncertainty reduction  
575 reported here for our standard inversion is likely may be higher than it would be if we accounted  
576 for b.c. uncertainties.

577 We conducted a test inversion for July (1.57  $\mu\text{m}$  and 0.5 ppm error case) in which b.c. are  
578 added as parameters (specifically, weekly average  $\text{CO}_2$  mixing ratios over each of the four lateral

Formatted: Subscript

579 walls of the domain) to be estimated in the state, with corresponding elements added to the  
580 Jacobian. Given that the actual Jacobian values are not available, we prescribed values that are  
581 somewhat realistic: 0.5 ppm ppm<sup>-1</sup> if an observation occurs in the same week as or after a b.c.,  
582 and 0 if an observation occurs before a b.c. We assumed a priori uncertainties of 1 ppm for the  
583 b.c., with no correlations among b.c. uncertainties or between b.c. and flux uncertainties. As  
584 expected, the reductions in flux uncertainty are smaller than the ones reported above, although  
585 the differences are only a factor of 0.01 or less. Weekly uncertainties for the b.c. are reduced by  
586 7-13%. A different experimental setup (e.g. larger Jacobian values for the b.c. or a larger  
587 number of disaggregated b.c. parameters) could potentially result in a much larger effect on the  
588 flux uncertainty reductions.

589 ~~The magnitude of b.c. errors can be substantial.~~—In addition to containing random errors,  
590 b.c. can also be a source of systematic errors. For example, Gourdji et al. [2012] found that two  
591 plausible sets of b.c. around North America generated inferred fluxes that differed by 0.7-0.9 Pg  
592 C/yr on the annual, continental scale (which is a very large amount compared to the annual a  
593 posteriori uncertainties for North America of 0.04-0.08 Pg C yr<sup>-1</sup> that we estimated in our OSSE  
594 (Figure 1Q4a)). They concluded that b.c. errors may be the primary control on flux errors in  
595 regional inversions at this coarse scale, while other factors such as flux resolution, priors, and  
596 model transport are more important at sub-domain scales.

597 Sparseness of observations has been a major cause of uncertainty in the boundary  
598 influence in previous regional inversions. Lauvaux et al. [2012], who conducted mesoscale  
599 inversions for the U.S. Midwest using tower measurements, found b.c. errors to be a significant  
600 source of uncertainty in the C budget over 7 months. They estimated that a potential bias of 0.55  
601 ppm in their b.c. translates into a flux error of 24 Tg C over 7 months in their 1000 km x 1000



602 km domain. Although they applied corrections to the model-derived b.c. using weekly aircraft  
603 profiles at four locations near their domain boundaries, they stated that the b.c. uncertainties  
604 were still large given the limited duration (a few hours per week) and spatial extent of the  
605 airborne observations, and concluded that additional observations would be necessary to reduce  
606 the uncertainties. ASCENDS is promising in this respect, as it (along with other satellites) will  
607 provide more frequent and widespread observations of concentrations at regional boundaries,  
608 possibly ~~lowering lessening~~ the role of b.c. in the overall C budget uncertainty to a minor one.  
609 ASCENDS observations could specifically be used in a global CO<sub>2</sub> data assimilation system to  
610 provide accurate b.c. for the regional flux inversion.

611 Posterior uncertainties are generally sensitive to the assumed prior uncertainties, although  
612 one might expect the sensitivity to not be so great in the case of a dense observational data set  
613 such as the one examined here. We test this hypothesis with an alternative prior uncertainty  
614 estimate, one that is uniformly larger than that for the standard inversion by a factor of 2. Figure  
615 11a-d shows the ratio of the posterior uncertainty for the large-priors inversion to that for the  
616 standard inversion, normalized by a factor of 2. Large areas of the domain have ratios  
617 significantly less than 1, especially in July and October. Where the ratio is close to 1, the  
618 posterior uncertainty is sensitive to the prior, indicating that the observations have a relatively  
619 weak influence; where the ratio is significantly less than 1, the posterior uncertainty is not so  
620 sensitive to the prior. The test demonstrates that the posterior uncertainty in many areas is not  
621 highly sensitive to the prior uncertainty and is strongly influenced by the observations.  
622 However, the sensitivity is high in the tundra and the desert, due to the tight (small) prior  
623 constraints in those regions (Figure 3).

624 Although the posterior uncertainty is not highly sensitive to the prior in all areas, it still  
625 increases everywhere in the large-priors inversion relative to the standard inversion, implying  
626 that our findings regarding whether or not the observations meet the target requirement (Section  
627 4.1) are dependent on the assumed priors. However, our standard priors are already enlarged  
628 uniformly by a factor of 4 relative to one set of prior uncertainty estimates, and they would have  
629 to be enlarged further over large areas to substantially increase biome-level posterior  
630 uncertainties. In addition, the larger the prior uncertainties are, the larger the uncertainty  
631 reductions are in general. Wherever the posterior uncertainty increases by a smaller factor than  
632 does the prior uncertainty (e.g. where the ratio is less than 1 in Figure 11), the uncertainty  
633 reduction increases. Altogether, the results of this sensitivity test suggest that it is important to  
634 consider different measures of the impact of observations on flux estimates, such as posterior  
635 uncertainty and uncertainty reduction, as we have done in this OSSE, given that different  
636 measures can be affected differently by assumptions such as prior uncertainties.

637 The inversion results are potentially sensitive to the assumed a priori flux error  
638 correlation lengths, with longer correlation lengths leading to more smooth uncertainty reduction  
639 patterns and larger uncertainty reductions. Rodgers [2000] shows that the inclusion of a priori  
640 error correlations can result in more “degrees of freedom for signal,” i.e. more information  
641 provided by the measurements on the unknowns. We carried out a test with alternative values  
642 for the correlation lengths derived from the study by Chevallier et al. [2012]—a shorter spatial  
643 correlation length of 200 km and a longer temporal correlation length of 35 days, for all months.  
644 (We estimated these values from Figure 5a and b of Chevallier et al. for the ~100 km and 7-day  
645 aggregation of our inversion.) The resulting uncertainty reductions are smaller everywhere than  
646 those in our standard inversion at the grid scale, with values of up to 40% in July and up to 15%

Formatted: Not Highlight

Formatted: Not Highlight

647 in January for Case 1 (compared to 45% and 25%, respectively, in the standard inversion).  
648 Apparently, the decrease in the spatial correlation length relative to the standard inversion has a  
649 larger effect than the increase in the temporal correlation length. Aggregated to the continent  
650 and month, the uncertainty reduction is less than that for the standard inversion for all months  
651 except July, for which the uncertainty reduction is marginally larger (Table 2). For July, the  
652 impact of the much longer temporal correlation length relative to the standard inversion on the  
653 aggregated result more than offsets that of the slightly shorter spatial correlation length. The  
654 annual uncertainty reduction for the alternative inversion is slightly larger than that for the  
655 standard inversion, because of the disproportionate influence of July, with its large a priori  
656 uncertainty. We conclude that our inversion results vary moderately given two reasonable sets  
657 of estimates for the a priori spatiotemporal error correlation lengths.

658

#### 659 4.3. Other Sources of Error

660 This analysis did not evaluate the impact of potential systematic errors (biases) in the  
661 observations or the transport model, which are not well represented by the Gaussian errors  
662 assumed in traditional linear error analysis [Baker et al., 2010]. Chevallier et al. [2007]  
663 demonstrated that potential biases in OCO satellite CO<sub>2</sub> measurements related to the presence of  
664 aerosols can completely negate the improvements to prior uncertainties provided by the  
665 measurements for the most polluted land regions and for ocean regions. In another OCO OSSE,  
666 Baker et al. [2010] found that a combination of systematic errors from aerosols, model transport,  
667 and incorrectly-assumed statistics could degrade both the magnitude and spatial extent of  
668 uncertainty improvements by about a factor of two over land, and even more over the ocean.  
669 Thus, it will be important to control systematic errors in ASCENDS observations and the

670 transport model as well as minimizing random errors. Note that systematic observation errors  
671 can be expected to decrease over the course of the mission as adjustments are made to the  
672 measurement system and to the retrieval algorithms in calibration/validation activities.

673

#### 674 4.4. Other Considerations in Evaluating ASCENDS

675 The potential combined use of multiple wavelengths in the ASCENDS measurements,  
676 e.g., various offsets from 1.57  $\mu\text{m}$ , could provide additional information on surface fluxes given  
677 the sensitivities to concentrations at different levels of the atmosphere. Furthermore, other  $\text{CO}_2$   
678 datasets will certainly be available alongside the ASCENDS data (e.g. from in situ networks),  
679 and the combination of datasets will provide stronger constraints on fluxes than any individual  
680 dataset [Hungershoefer et al., 2010].

681 Our comparison of the results for the 1.57 and 2.05  $\mu\text{m}$  wavelengths over North America  
682 may be less applicable to other parts of the world. The global OSSE study by Hungershoefer et  
683 al. [2010], which compared various observing systems, including a satellite lidar system similar  
684 to ASCENDS, A-SCOPE, found that the 1.6  $\mu\text{m}$  wavelength results in larger uncertainty  
685 reductions over South America while performing less well than 2.0  $\mu\text{m}$  over temperate and cold  
686 regions. They attribute the better performance of 1.6  $\mu\text{m}$  over South America to the strong  
687 vertical mixing of air there, which lessens the disadvantage of that wavelength's having weaker  
688 sensitivity to the lower troposphere. (However, they used a simpler error formulation.) On the  
689 other hand, in our global inversion, 2.05  $\mu\text{m}$  results in larger uncertainty reductions than 1.57  $\mu\text{m}$   
690 throughout the world, by 8% on average (for RRV error of 0.5-1.0 ppm).

691

692

693 **5. Conclusions**

694 We have conducted an observing system simulation for North America, using projected  
695 ASCENDS observation uncertainty estimates and a novel approach utilizing a portable footprint  
696 library generated from a high-resolution Lagrangian transport model, to quantify the surface CO<sub>2</sub>  
697 flux constraints provided by the future observations. We consider four possible configurations  
698 for the active optical remote sensing instrument covering two weighting functions and two  
699 random error levels. We find that the ASCENDS observations potentially reduce flux  
700 uncertainties substantially at fine and biome scales. At the 1° x 1° grid scale, weekly uncertainty  
701 reductions up to 30-45% (averaged over the year) are achieved depending on the presumed  
702 instrument configuration. Relatively large uncertainty reductions occur year-round in southern  
703 Mexico and the ~~U.S.~~ Pacific Northwest and seasonally in the southeastern and mid-western U.S.  
704 and parts of Canada and Alaska, when and where there is good coverage by observations with  
705 low uncertainties and a priori uncertainties are large. Uncertainty reductions at the annual,  
706 biome scale range from ~40% to ~75% across the four experimental cases, and from ~65% to  
707 ~85% for the continent as a whole. The uncertainty reductions for the 1.57 μm candidate  
708 wavelength are on average 10% smaller than those for 2.05 μm across the biomes and the two  
709 RRV reference error levels, and for 0.5 ppm RRV ~~reference~~ error are on average ~25% larger  
710 than those for 1.0 ppm error across biomes and the two wavelengths.

711 ~~Our uncertainty reductions are substantially smaller than those of a global ASCENDS~~  
712 ~~inversion at the 4.5° x 6° scale of the latter's model grid and at the biome scale. The global~~  
713 ~~inversion benefits from the use of observations located around the world rather than in a limited~~  
714 ~~region, and it has fewer unknowns to be solved for within North America. On the other hand,~~  
715 ~~inversions at higher resolution enable investigation of biospheric and other processes at the finer~~

716 ~~scales that are needed to understand the mechanisms for inferred CO<sub>2</sub> flux variability and trends.~~  
717 ~~In addition, by reducing aggregation error, higher resolution inversions can produce flux~~  
718 ~~estimates with less systematic error than those of lower resolution inversions when aggregated to~~  
719 ~~the same scale.~~

720 Based on the flux precision on an annual, biome scale suggested by Hungershoefer et al.  
721 [2010] for understanding the global carbon sink and feedbacks, ASCENDS observations would  
722 meet a threshold requirement for all biomes within the range of measurement designs considered  
723 here. The observations constrain a posteriori uncertainties to a level of 0.01-0.06 Pg C yr<sup>-1</sup>, and  
724 could thus help pin down the location and magnitude of long-term C sinks. With regards to the  
725 more stringent target requirement, a subset of the instrument designs would meet the target for a  
726 majority of biomes.

727 The results we have presented may be optimistic, as ~~uncertainties in boundary conditions~~  
728 ~~and~~ potential systematic errors in the observations, boundary conditions, and transport model that  
729 we have neglected would degrade the flux estimates. Modifications to the size and location of  
730 our regional domain, however, e.g. an eastward shift, could improve the constraints by satellite  
731 observations on North American fluxes. In addition, our consideration of different measures of  
732 the impact of observations on flux estimates, such as posterior uncertainty and uncertainty  
733 reduction, strengthens the study, given that different measures can be affected differently by  
734 assumptions such as prior uncertainties.

735 In future work, inversions in various regions (including, for example, South America)  
736 with a more comprehensive treatment of error sources could more definitively establish the  
737 usefulness of ASCENDS observations for constraining fluxes at fine and large scales and  
738 answering global carbon cycle science questions.

739

740

741 **Acknowledgments**

742 Work at NASA and AER has been supported by the NASA Atmospheric CO<sub>2</sub> Observations from  
743 Space program element and NASA ASCENDS Pre-Phase A activity funding. We are grateful to  
744 the NASA Ames HEC facility staff for assistance in executing the WRF-STILT runs on the  
745 Pleiades supercomputer, and to the NASA HEC Program for granting use of the Dali and  
746 Discover systems at the NASA Center for Climate Simulation. We also thank J. Abshire, E.  
747 Browell, and R. Menzies for contributions to ASCENDS data characterization, G. J. Collatz for  
748 making available the CASA-GFED fluxes that we used to construct the a priori uncertainties, R.  
749 Aschbrenner for help with the footprint calculations, S. Gourdji for providing correlation  
750 parameters and the biome map, P. Rayner and A. Michalak for advice on inversions, M. Manyin  
751 and Y. Liu for computing help, L. Ott for help with transferring WRF-STILT files, and G. J.  
752 Collatz and E. McGrath-Spangler for comments on the manuscript. Finally, we appreciate the  
753 comments provided by two anonymous referees.

754

Formatted: Font: Not Bold

755 **References**

756

757 Baker, D. F., Boesch, H., Doney, S. C., O'Brien, D., and Schimel, D. S. (2010), Carbon  
758 source/sink information provided by column CO<sub>2</sub> measurements from the Orbiting Carbon  
759 Observatory, *Atmos. Chem. Phys.*, 10, 4145–4165, doi:10.5194/acp-10-4145-2010.

760 Basu, S., S. Guerlet, A. Butz, S. Houweling, O. Hasekamp, I. Aben, P. Krummel, P. Steele, R.  
761 Langenfelds, M. Torn, S. Biraud, B. Stephens, A. Andrews, and D. Worthy (2013), Global  
762 CO<sub>2</sub> fluxes estimated from GOSAT retrievals of total column CO<sub>2</sub>, *Atmos. Chem. Phys.*, 13,  
763 8695–8717, doi:10.5194/acp-13-8695-2013.

764 [Bocquet, M., Wu, L., Chevallier, F. 2011. Bayesian design of control space for optimal](#)  
765 [assimilation of observations. Part I: Consistent multiscale formalism. \*Q. J. R. Meteorol. Soc.\*](#)  
766 [137: 1340–1356. doi:10.1002/qj.837.](#)

767 [Brioude, J., Kim, S.-W., Angevine, W. M., Frost, G. J., Lee, S-H, McKeen, S. A., Trainer, M.,](#)  
768 [Fehsenfeld, F. C., Holloway, J. S., Ryerson, T. B., Williams, E. J., Petron, G., and Fast, J. D.](#)  
769 [\(2011\). Top-down estimate of anthropogenic emission inventories and interannual variability](#)  
770 [in Houston using a mesoscale inverse modeling technique, \*J. Geophys. Res.\*, 116, D20305,](#)  
771 [doi:10.1029/2011JD016215.](#)

772 [Brioude, J., Petron, G., Frost, G. J., Ahmadov, R., Angevine, W. M., Hsie, E. -Y., Kim, S. -W.,](#)  
773 [Lee, S. -H., McKeen, S. A., Trainer, M., Fehsenfeld, F. C., Holloway, J. S., Peischl, J.,](#)  
774 [Ryerson, T. B., and Gurney, K. R. \(2012\). A new inversion method to calculate emission](#)  
775 [inventories without a prior at mesoscale: Application to the anthropogenic CO<sub>2</sub> emission](#)  
776 [from Houston, Texas, \*J. Geophys. Res.\*, 117, D05312, doi:10.1029/2011JD016918.](#)

777 [Brioude, J., Angevine, W. M., Ahmadov, R., Kim, S. -W., Evan, S., McKeen, S. A., Hsie, E. -Y.,](#)  
778 [Frost, G. J., Neuman, J. A., Pollack, I. B., Peischl, J., Ryerson, T. B., Holloway, J., Brown, S.](#)

Formatted: Subscript



779 [S., Nowak, J. B., Roberts, J. M., Wofsy, S. C., Santoni, G. W., Oda, T., and Trainer, M.](#)  
780 [\(2013\). Top-down estimate of surface flux in the Los Angeles Basin using a mesoscale](#)  
781 [inverse modeling technique: assessing anthropogenic emissions of CO, NO<sub>x</sub> and CO<sub>2</sub> and](#)  
782 [their impacts, Atmos. Chem. Phys., 13, 3661-3677, doi:10.5194/acp-13-3661-2013.](#)

Formatted: Subscript

Formatted: Subscript

783 Butler, M. P., Davis, K. J., Denning, A. S., and Kawa, S. R. (2010), Using continental  
784 observations in global atmospheric inversions of CO<sub>2</sub>: North American carbon sources and  
785 sinks, *Tellus*, 62B, 550–572, doi:10.1111/j.1600-0889.2010.00501.x.

786 Caron, J. and Y. Durand (2009), Operating wavelengths optimization for a spaceborne lidar  
787 measuring atmospheric CO<sub>2</sub>, *Appl. Opt.* 48, 5413-5422.

788 Chevallier, F., F.-M. Bréon, and P. J. Rayner (2007), Contribution of the Orbiting Carbon  
789 Observatory to the estimation of CO<sub>2</sub> sources and sinks: Theoretical study in a variational  
790 data assimilation framework, *J. Geophys. Res.*, 112, D09307, doi:10.1029/2006JD007375.

791 Crisp, D., Miller, C. E., and DeCola, P. L. (2008), NASA Orbiting Carbon Observatory:  
792 measuring the column averaged carbon dioxide mole fraction from space, *J. Appl. Remote*  
793 *Sens.*, 2, 023508, doi:10.1117/1.2898457.

794 [Deng, F., D. B. A. Jones, D. K. Henze, N. Bousseres, K. W. Bowman, J. B. Fisher, R. Nassar, C.](#)  
795 [O'Dell, D. Wunch, P. O. Wennberg, E. A. Kort, S. C. Wofsy, T. Blumenstock, N. M.](#)  
796 [Deutscher, D. W. T. Griffith, F. Hase, P. Heikkinen, V. Sherlock, K. Strong, R. Sussmann,](#)  
797 [and T. Warneke \(2014\), Inferring regional sources and sinks of atmospheric CO<sub>2</sub> from](#)  
798 [GOSAT XCO<sub>2</sub> data, Atmos. Chem. Phys., 14, 3703–3727, doi:10.5194/acp-14-3703-2014.](#)

Formatted: Subscript

Formatted: Subscript

799 Dlugokencky, E.J., P.M. Lang, K.A. Masarie, A.M. Crotwell, and M.J. Crotwell (2013),  
800 Atmospheric Carbon Dioxide Dry Air Mole Fractions from the NOAA ESRL Carbon Cycle

801 Cooperative Global Air Sampling Network, 1968-2012, Version: 2013-08-28, Path:  
802 ftp://aftp.cmdl.noaa.gov/data/trace\_gases/co2/flask/surface/.

803 Eldering, A., Solish, B., Kahn, P., Boland, S., Crisp, D., and Gunson, M. (2012), High Precision  
804 Atmospheric CO<sub>2</sub> Measurements from Space: The Design and Implementation of OCO-2,  
805 IEEE Aerospace Conference Proceedings, 1805-1814.

806 Engelen, R. J., Denning, A. S., and Gurney, K. R.: On error estimation in atmospheric CO<sub>2</sub>  
807 inversions, *J. Geophys. Res.*, *107*, 4635, doi:10.1029/2002JD002195, 2002.

808 Enting, I. G., Trudinger, C. M. and Francey, R. J. (1995), A synthesis inversion of the  
809 concentration and  $\delta^{13}\text{C}$  of atmospheric CO<sub>2</sub>. *Tellus 47B*, 35–52.

810 Feng, L., Palmer, P. I., Boesch, H., and Dance, S.: Estimating surface CO<sub>2</sub> fluxes from space-  
811 borne CO<sub>2</sub> dry air mole fraction observations using an ensemble Kalman Filter, *Atmos.*  
812 *Chem. Phys.*, *9*, 2619–2633, doi:10.5194/acp-9-2619-2009, 2009.

813 Gerbig, C., J. C. Lin, S. C. Wofsy, B. C. Daube, A. E. Andrews, B. B. Stephens, P. S. Bakwin,  
814 and C. A. Grainger (2003), Towards constraining regional scale fluxes of CO<sub>2</sub> with  
815 atmospheric observations over a continent: 2. Analysis of COBRA data using a receptor-  
816 oriented framework, *J. Geophys. Res.*, *108* (D24), 4757, doi:10.1029/2003JD003770.

817 Göckede, M., Michalak, A. M., Vickers, D., Turner, D. P., and Law, B. E.: Atmospheric inverse  
818 modeling to constrain regional scale CO<sub>2</sub> budgets at high spatial and temporal resolution, *J.*  
819 *Geophys. Res.*, *115*, D15113, doi:10.1029/2009JD012257, 2010a.

820 Göckede, M., D. P. Turner, A. M. Michalak, D. Vickers, and B. E. Law (2010b), Sensitivity of a  
821 subregional scale atmospheric inverse CO<sub>2</sub> modeling framework to boundary conditions, *J.*  
822 *Geophys. Res.*, *115*, D24112, doi:10.1029/2010JD014443.

Formatted: Font: Not Italic

823 Gourdj, S. M., K. L. Mueller, V. Yadav, D. N. Huntzinger, A. E. Andrews, M. Trudeau, G.  
824 Petron, T. Nehrkorn, J. Eluszkiewicz, J. Henderson, D. Wen, J. Lin, M. Fischer, C. Sweeney,  
825 and A. M. Michalak (2012), North American CO<sub>2</sub> exchange: intercomparison of modeled  
826 estimates with results from a fine-scale atmospheric inversion, *Biogeosciences*, *9*, 457–475.  
827 Gurney, K.R., D.L. Mendoza, Y. Zhou, M.L. Fischer, C.C. Miller, S. Geethakumar, and S. de la  
828 Rue du Can (2009), High Resolution Fossil Fuel Combustion CO<sub>2</sub> Emission Fluxes for the  
829 United States, *Environ. Sci. & Technol.* *43* (14), 5535-5541, doi:10.1021/es900806c.  
830 Houweling, S., F.-M. Breon, I. Aben, C. Roedenbeck, M. Gloor, M. Heimann, and P. Ciais  
831 (2004), Inverse modeling of CO<sub>2</sub> sources and sinks using satellite data: a synthetic inter-  
832 comparison of measurement techniques and their performance as a function of space and  
833 time, *Atmos. Chem. Phys.*, *4*, 523–538.  
834 Hungershofer, K., F.-M. Breon, P. Peylin, F. Chevallier, P. Rayner, A. Klonecki, S. Houweling,  
835 and J. Marshall (2010), Evaluation of various observing systems for the global monitoring of  
836 CO<sub>2</sub> surface fluxes, *Atmos. Chem. Phys.*, *10*, 10503–10520, doi:10.5194/acp-10-10503-2010.  
837 Huntzinger, D. N., Post, W. M., Wei, Y., Michalak, A. M., West, T. O., Jacobson, A. R., Baker,  
838 I. T., Chen, J. M., Davis, K. J., Hayes, D. J., Hoffman, F. M., Jain, A. K., Liu, S., McGuire,  
839 A. D., Neilson, R. P., Potter, C., Poulter, B., Price, D., Raczka, B. M., Tian, H. Q., Thornton,  
840 P., Tomelleri, E., Viovy, N., Xiao, J., Yuan, W., Zeng, N., Zhao, M., and Cook, R.: North  
841 American Carbon Program (NACP) Regional Interim Synthesis: Terrestrial Biospheric  
842 Model Intercomparison, *Ecol. Model.*, *232*, 144–157, doi:10.1016/j.ecolmodel.2012.02.004,  
843 2012.  
844 Hu, Y., K. Starnes, M. Vaughan, J. Pelon, C. Weimer, D. Wu, M. Cisewski, W. Sun, P. Yang,  
845 B. Lin, A. Omar, D. Flittner, C. Hostetler, C. Trepte, D. Winker, G. Gibson, and M. Santa-

846 Maria, Sea surface wind speed estimation from space-based lidar measurements, *Atmos.*  
847 *Chem. Phys.*, 8, 3593-3601, 2008.

848 Ingmann, P.: A-SCOPE, Advanced space carbon and climate observation of planet earth, Report  
849 for Assessment, SP-1313/1, ESA communication production office, Noordwijk, The  
850 Netherlands, 2008.

851 Kaminski, T., Rayner, P., Heimann, M., and Enting, I.: On aggregation errors in atmospheric  
852 transport inversions, *J. Geophys. Res.*, 106(D5), 4703–4715, 2001.

853 Kaminski, T., Scholze, M. and Houweling, S.: Quantifying the benefit of A-SCOPE data for  
854 reducing uncertainties in terrestrial carbon fluxes in CCDAS, *Tellus*, 62B(5), 784–796, 2010.

855 Kawa, S. R., D. J. Erickson III, S. Pawson, and Z. Zhu (2004), Global CO<sub>2</sub> transport simulations  
856 using meteorological data from the NASA data assimilation system, *J. Geophys. Res.*, 109,  
857 D18312, doi:10.1029/2004JD004554.

858 Kawa, S. R., J. Mao, J. B. Abshire, G. J. Collatz, X. Sun, and C. J. Weaver (2010), Simulation  
859 studies for a space-based CO<sub>2</sub> lidar mission, *Tellus B*, doi:10.1111/j.1600-  
860 0889.2010.00486.x.

861 Kort, E. A. et al. (2008), Emissions of CH<sub>4</sub> and N<sub>2</sub>O over the United States and Canada based on  
862 a receptor-oriented modeling framework and COBRA-NA atmospheric observations,  
863 *Geophys. Res. Lett.*, 35, L18808, doi:10.1029/2008GL034031.

864 Kort E. A. et al. (2010), Atmospheric constraints on 2004 emissions of methane and nitrous  
865 oxide in North America from atmospheric measurements and receptor-oriented modeling  
866 framework, *J. Integr. Environ. Sci.*, 7:2, 125-133.

867 Lauvaux, T., A. E. Schuh, M. Uliasz, S. Richardson, N. Miles, A. E. Andrews, C. Sweeney, L. I.  
868 Diaz, D. Martins, P. B. Shepson, and K. J. Davis: Constraining the CO<sub>2</sub> budget of the corn

869 belt: exploring uncertainties from the assumptions in a mesoscale inverse system, *Atmos.*  
870 *Chem. Phys.*, 12, 337–354, doi:10.5194/acp-12-337-2012, 2012.

871 Le Quéré, C., Andres, R. J., Boden, T., Conway, T., Houghton, R. A., House, J. I., Marland, G.,  
872 Peters, G. P., van der Werf, G., Ahlström, A., Andrew, R. M., Bopp, L., Canadell, J. G.,  
873 Ciais, P., Doney, S. C., Enright, C., Friedlingstein, P., Huntingford, C., Jain, A. K.,  
874 Jourdain, C., Kato, E., Keeling, R. F., Klein Goldewijk, K., Levis, S., Levy, P., Lomas, M.,  
875 Poulter, B., Raupach, M. R., Schwinger, J., Sitch, S., Stocker, B. D., Viovy, N., Zaehle, S.,  
876 and Zeng, N.: The global carbon budget 1959–2011, *Earth Syst. Sci. Data Discuss.*, 5, 1107-  
877 1157, doi:10.5194/essdd-5-1107-2012, 2012.

878 Lin, J. C., C. Gerbig, S. C. Wofsy, B. C. Daube, A. E. Andrews, K. J. Davis, and C. A. Grainger  
879 (2003), A near-field tool for simulating the upstream influence of atmospheric observations:  
880 The Stochastic Time-Inverted Lagrangian Transport (STILT) model, *J. Geophys. Res.*,  
881 *108(D16)*, 4493, doi:10.1029/2002JD003161.

882 McKain, K., S. C. Wofsy, T. Nehrkorn, J. Eluszkiewicz, J. R. Ehleringer, and B. B. Stephens  
883 (2012), Assessment of ground-based atmospheric observations for verification of greenhouse  
884 gas emissions from an urban region, *Proc. Natl. Acad. Sci.*, 109, 8423-8428.

885 Miller, S. M. E. A. Kort, A. I. Hirsch, E. J. Dlugokencky, A. E. Andrews, X. Xu, H. Tian, T.  
886 Nehrkorn, J. Eluszkiewicz, A. M. Michalak, and S. C. Wofsy (2012) Regional sources of  
887 nitrous oxide over the United States: Seasonal variation and spatial distribution, *J. Geophys.*  
888 *Res.*, 117, D06310, doi:10.1029/2011JD016951.

889 Miller, S. M., S. C. Wofsy, A. M. Michalak, E. A. Kort, A. E. Andrews, S. C. Biraud, E. J.  
890 Dlugokencky, J. Eluszkiewicz, M. L. Fischer, G. Janssens-Maenhout, B. R. Miller, J. B.  
891 Miller, S. A. Montzka, T. Nehrkorn, and C. Sweeney (2013), Anthropogenic emissions of

892 methane in the United States, *Proc. Natl. Acad. Sci.*, 110(50), 20018-20022,  
893 doi:10.1073/pnas.1314392110.

894 National Research Council (2007), *Earth Science and Applications from Space: National*  
895 *Imperatives for the Next Decade and Beyond*. Washington, DC: The National Academies  
896 Press.

897 Nehr Korn, T., J. Eluszkiewicz, S. C. Wofsy, J. C. Lin, C. Gerbig, M. Longo, and S. Freitas  
898 (2010), Coupled Weather Research and Forecasting/Stochastic Time-Inverted Lagrangian  
899 Transport (WRF-STILT) model, *Meteor. Atmos. Phys.*, 107 (1-2), 51–64,  
900 doi:10.1007/s00703-010-0068-x.

901 Olson, D. M., Dinerstein, E., Wikramanayake, E. D., Burgess, N. D., Powell, G. V. N.,  
902 Underwood, E. C., D'Amico, J. A., Itoua, I., Strand, H. E., Morrison, J. C., Loucks, C. J.,  
903 Allnutt, T. F., Ricketts, T. H., Kura, Y., Lamoreux, J. F., Wettengel, W. W., Hedao, P., and  
904 Kassem, K. R.: Terrestrial ecoregions of the world: a new map of life on earth, *Bioscience*,  
905 51, 933–938, 2001.

906 Peters, W., A. R. Jacobson, C. Sweeney, A. E. Andrews, T. J. Conway, K. Masarie, J. B. Miller,  
907 L. M. P. Bruhwiler, G. Petron, A. I. Hirsch, D. E. J. Worthy, G. R. van der Werf, J. T.  
908 Randerson, P. O. Wennberg, M. C. Krol, and P. P. Tans (2007), An atmospheric perspective  
909 on North American carbon dioxide exchange: Carbon Tracker, *Proc. Nat. Acad. Sci.*, 104,  
910 18,925-18,930.

911 Pillai, D., Gerbig, C., Marshall, J., Ahmadov, R., Kretschmer, R., Koch, T., and Karstens, U.:  
912 High resolution modeling of CO<sub>2</sub> over Europe: implications for representation errors of  
913 satellite retrievals, *Atmos. Chem. Phys.*, 10, 83–94, doi:10.5194/acp-10-83-2010, 2010.

914 Randerson, J. T., M. V. Thompson, and C. M. Malmstrom (1996), Substrate limitations for  
915 heterotrophs: Implications for models that estimate the seasonal cycle of atmospheric CO<sub>2</sub>,  
916 *Global Biogeochem. Cycles*, *10*, 585-602.

917 Rayner, P. J., Enting, I. G., Francey, R. J. and Langenfelds, R. 1999. Reconstructing the recent  
918 carbon cycle from atmospheric CO<sub>2</sub>, δ<sup>13</sup>C and O<sub>2</sub>/N<sub>2</sub> observations. *Tellus* **51B**, 213–232.

919 Rayner, P. J., and D. M. O'Brien (2001), The utility of remotely sensed CO<sub>2</sub> concentration data  
920 in surface source inversions, *Geophys. Res. Lett.*, *28*, 175–178.

921 Rienecker, M. M., et al.: MERRA: NASA's Modern-Era Retrospective Analysis for Research  
922 and Applications, *J. Climate*, *24*, 3624–3648, 2011.

923 Rodgers, C. D. (2000), *Inverse Methods for Atmospheric Sounding: Theory and Practice*. World  
924 Scientific.

925 Schuh, A. E., Denning, A. S., Corbin, K. D., Baker, I. T., Uliasz, M., Parazoo, N., Andrews, A.  
926 E., and Worthy, D. E. J. (2010), A regional high-resolution carbon flux inversion of North  
927 America for 2004, *Biogeosciences*, *7*, 1625–1644, doi:10.5194/bg-7-1625-2010.

928 Skamarock, W. C. and J. B. Klemp (2008), A time-split nonhydrostatic atmospheric model for  
929 weather research and forecasting applications, *J. Comp. Phys.*, *227*, 3465-3485.

930 van der Werf, G. R., J. T. Randerson, L. Giglio, G. J. Collatz, P. S. Kasibhatla, and A. F.  
931 Arellano, Jr (2006), Interannual variability in global biomass burning emissions from 1997-  
932 2004, *Atmos. Chem. Phys.*, *6*, 3423-3441.

933 van der Werf, G. R., J. T. Randerson, L. Giglio, G. J. Collatz, M. Mu, P. S. Kasibhatla, D. C.  
934 Morton, R. S. DeFries, Y. Jin, and T. T. van Leeuwen (2010), Global fire emissions and the  
935 contributions of deforestation, savanna, forest, agricultural, and peat fires (1997-2009),  
936 *Atmos. Chem. Phys.*, *10*, 11707-11735, doi:10.5194/acp-10-11707-2010.

937 Wang, J. S., M. B. McElroy, J. A. Logan, P. I. Palmer, W. L. Chameides, Y. Wang, and I. A.  
938 Megretskaia (2008), A quantitative assessment of uncertainties affecting estimates of global  
939 mean OH derived from methyl chloroform observations, *J. Geophys. Res.*, *113*, D12302,  
940 doi:10.1029/2007JD008496.

941 Yokota, T., Yoshida, Y., Eguchi, N., Ota, Y., Tanaka, T., Watanabe, H., and Maksyutov, S.  
942 (2009), Global Concentrations of CO<sub>2</sub> and CH<sub>4</sub> Retrieved from GOSAT: First Preliminary  
943 Results, *SOLA*, *5*, 160–163, doi:10.2151/sola.2009-041.

944 Zhao, C., A. E. Andrews, L. Bianco, J. Eluszkiewicz, A. Hirsch, C. MacDonald, T. Nehrkorn,  
945 and M. L. Fischer (2009), Atmospheric inverse estimates of methane emissions from Central  
946 California, *J. Geophys. Res.*, *114*, D16302, doi:10.1029/2008JD011671.

947



948 **Table 1.** Spatiotemporal Correlation Parameters Used.

Month	Spatial correlation e-folding length (km)	Temporal correlation e-folding length (days)
January	481	17.2
April	419	7.2
July	284	6.9
October	638	1.6

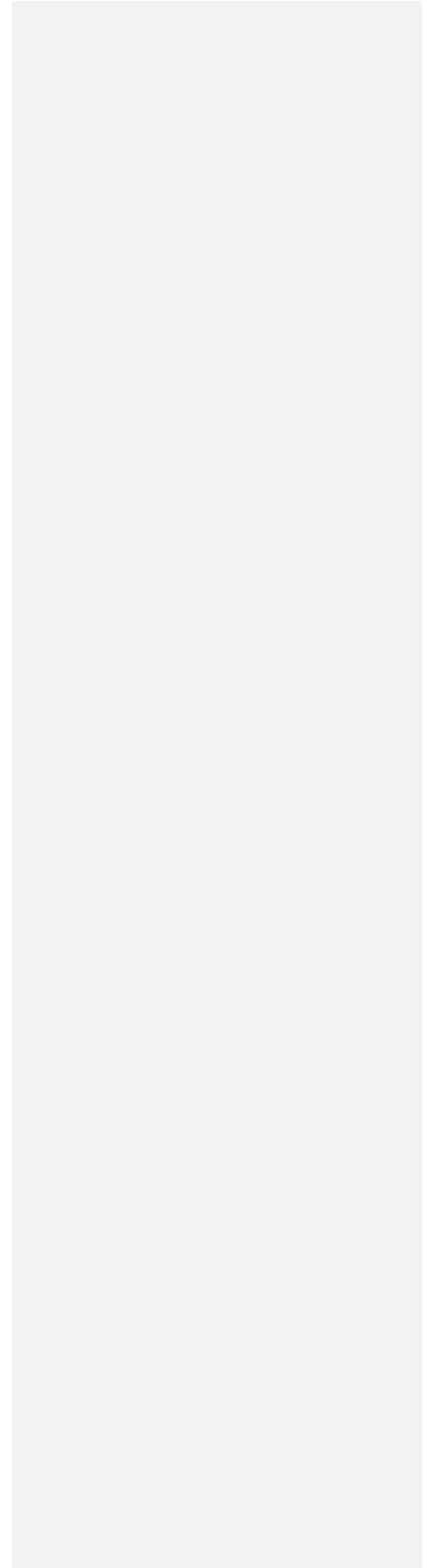
949

950 **Table 2.** Flux Uncertainties Aggregated to Entire Continent and Month or Year (Pg C yr<sup>-1</sup>).

	January	April	July	October	Annual
<u>Standard inversion</u>					
A priori	0.42	0.78	1.26	0.82	0.24
A posteriori (uncertainty reduction)					
Case 1	0.24 (43%)	0.17 (78%)	0.15 (88%)	0.2 (76%)	0.05 (78%)
Case 2	0.33 (21%)	0.28 (65%)	0.26 (80%)	0.31 (61%)	0.08 (66%)
Case 3	0.18 (57%)	0.13 (83%)	0.12 (91%)	0.15 (81%)	0.04 (83%)
Case 4	0.28 (35%)	0.22 (72%)	0.2 (84%)	0.25 (69%)	0.07 (73%)
<u>Inversion with alternative correl. lengths (200 km, 35 days)</u>					
A priori	0.23	0.59	1.27	0.59	0.21
A posteriori (uncertainty reduction)					
Case 1	0.17 (25%)	0.15 (74%)	0.14 (89%)	0.16 (73%)	0.04 (80%)

951

952



953 **Figure Captions**

954 **Figure 1.** Vertical weighting functions per ppmv of CO<sub>2</sub> ( $10^{-6}$  ppmv<sup>-1</sup> hPa<sup>-1</sup>) for two candidate  
955 ASCENDS wavelengths. These relate differential optical depth lidar measurements (on-line  
956 minus off-line) to column-average CO<sub>2</sub> mixing ratios. The precise on-line wavelengths used  
957 here are 1.571121 μm, which is 10 picometers (pm) offset from line center, and 2.051034 μm.

958 **Figure 2.** Examples of measurement locations (individual 10-s averages) and 10-s uncertainties  
959 ( $1\sigma$ ) for the 0.5 ppm RRV random error case, across 7 day spans for a) the 1.57 μm wavelength  
960 in January and b) in July; and for c) the 2.05 μm wavelength in January and d) in July.  
961 Locations with OD > 0.7 are rejected. e) Ratio of uncertainty for 2.05 μm to 1.57 μm in January  
962 and f) in July. The WRF domain for the runs utilized in this study is indicated by the bold, black  
963 lines in a).

964 **Figure 3.** A priori weekly flux uncertainty for a) January, b) April, c) July, and d) October.

965 Average fractional flux uncertainties over the domain are given in each panel (F ≡ flux).  $1 \mu\text{mol}$   
966  $\text{m}^{-2} \text{s}^{-1} = 1.037 \text{ g C m}^{-2} \text{ d}^{-1} = 4.4 \times 10^{-8} \text{ kg CO}_2 \text{ m}^{-2} \text{ s}^{-1}$ .

967 **Figure 4.** Footprint maps for one simulated ASCENDS measurement location (marked by black  
968 star) on January 1, 2007 at 18 UTC, integrated over 10 days and convolved over the 500-14500  
969 m AGL range with two candidate ASCENDS weighting functions: for the CO<sub>2</sub> laser lines at 2.05  
970 μm (top) and 1.57 μm (bottom). Units are ppm/(μmol/m<sup>2</sup>/s). Note that the native temporal  
971 resolution of the footprints is 3 hours; the 10-day integral in this figure is for illustrative purposes  
972 only. Only footprints over land are used in the analysis.

973 **Figure 5.** Jacobian values averaged over all observations and weekly flux intervals for a)  
974 January, b) April, c) July, and d) October, for the 1.57 μm weighting function.

Formatted: Subscript

975 **Figure 6.** A posteriori weekly flux uncertainty over a) January, b) April, c) July, and d) October,  
976 for Case 1 (1.57  $\mu\text{m}$  and 0.5 ppm RRV error). Shown here are RMS values from the first 4  
977 weeks of each month.  $1 \mu\text{mol m}^{-2} \text{s}^{-1} = 1.037 \text{ g C m}^{-2} \text{d}^{-1} = 4.4 \times 10^{-8} \text{ kg CO}_2 \text{ m}^{-2} \text{s}^{-1}$ .

978 **Figure 7.** Weekly fractional flux uncertainty reduction over a) January, b) April, c) July, and d)  
979 October, for Case 1 (1.57  $\mu\text{m}$  and 0.5 ppm RRV error). Shown here are results from the first 4  
980 weeks of each month.

981 **Figure 8.** Weekly fractional flux uncertainty reduction (RMS over the 4 months) for a) Case 1  
982 (1.57  $\mu\text{m}$  and 0.5 ppm RRV error), b) Case 2 (1.57  $\mu\text{m}$  and 1.0 ppm), c) Case 3 (2.05  $\mu\text{m}$  and 0.5  
983 ppm), and d) Case 4 (2.05  $\mu\text{m}$  and 1.0 ppm).

984 ~~**Figure 9.** a) Reduction in weekly flux uncertainty (RMS over 4 months) of the regional  
985 inversion, aggregated to  $4.5^\circ \times 6^\circ$  resolution, and b) the global inversion results, which include  
986 ocean grid cells as well as land. Results in both panels are for the 1.57  $\mu\text{m}$  wavelength and 0.5  
987 ppm error case.~~

988 **Figure 910.** Biomes used, taken from Olson et al. [2001] with modifications by Gourdji et al.  
989 [2012].

990 **Figure 101.** Results aggregated to biomes and continent, and compared with other studies. a) A  
991 priori and a posteriori uncertainties for the year, including results from Gourdji et al. [2012]. b)  
992 RMS of the four monthly uncertainties, including results from the global inversion. c) Fractional  
993 uncertainty reductions. d) Land area of the biomes. Gourdji et al. reported results for only the  
994 three biomes that were well constrained by their in situ observation network, along with results  
995 aggregated over the full continent; we show the approximate average of their "Simple" and  
996 "NARR" inversions. The figure does not include a priori uncertainties for Gourdji et al. since

997 | their method does not rely on a priori estimates. e) Fractional uncertainty reduction necessary to  
998 | meet the target requirement.

999 | Figure 11. Ratio of the posterior uncertainty for the 2× priors inversion to that for the standard  
1000 | inversion, normalized by a factor of 2, for Case 1 in a) January, b) April, c) July, and d) October.

Formatted: Font: Bold

Formatted: Font: Bold